

# Supporting Information

## Metal-organic frameworks as SERS substrates with high tailorability

Hongzhao Sun,<sup>1,2,§</sup> Shan Cong,<sup>1,3,§</sup> Zuhui Zheng<sup>1</sup>, Zhen Wang<sup>1</sup>, Zhigang Chen<sup>1</sup>, Zhigang Zhao<sup>1,4</sup>

<sup>1</sup>Key Lab of Nanodevices and Applications, Suzhou Institute of Nano-Tech and Nano-Bionics, Chinese

Academy of Sciences (CAS), Suzhou 215123, China

<sup>2</sup>Nano Science and Technology Institute, University of Science and Technology of China, Suzhou

215123, China

<sup>3</sup>Key Laboratory of Multifunctional Nanomaterials and Smart Systems, Chinese Academy of Sciences

(CAS), Suzhou 215123, China

<sup>4</sup>Division of Nanomaterials, Suzhou Institute of Nano-Tech and Nano-Bionics, Chinese Academy of

Sciences, Nanchang 330200, China

## Table of contents

### Experimental Section

Materials and Characterization	S5
Preparation of Samples	S6-8
Raman measurement	S9
Calculation of the enhancement factor	S10
Adsorption capacity measurement	S11
The reproducibility and statistical for statistical analysis	S11

**Figure. S1** FTIR spectra of cobalt-based MOFs with different organic linkers.

**Figure. S2** SERS spectra for R6G ( $10^{-6}$  M) on the ZIF-67 and Si/SiO<sub>2</sub> substrates.

**Figure. S3** R6G adsorption isotherm.

**Figure. S4-7** The intensities of the P<sub>1</sub> ( $612\text{ cm}^{-1}$ ) Raman vibration mode of R6G on different MOF substrates.

**Figure. S8** FTIR spectra of the Co-TCPP MOFs, Cu-TCPP MOFs, and Zn-TCPP MOFs.

**Figure. S9** SEM image of the ZIF-8 crystals.

**Figure. S10** The intensities of the P<sub>5</sub> ( $1115\text{ cm}^{-1}$ ) Raman vibration mode of MO on different ZIF-8 substrates.

**Figure. S11** PXRD patterns of WO<sub>3</sub>, W<sub>18</sub>O<sub>49</sub>, and WO<sub>2</sub> samples.

**Figure. S12** SERS spectra of R6G ( $10^{-6}$  M) and MO ( $10^{-4}$  M) on the WO<sub>x</sub> substrates

**Figure. S13** PXRD patterns of ZIF-67, acid-treated ZIF-67, and simulated ZIF-67 crystals, respectively.

**Figure. S14** SEM image of APTES@ZIF-67 crystals.

**Figure. S15** Raman spectrum of liquid-phase benzaldehyde.

**Figure. S16** N<sub>2</sub> adsorption-desorption isotherms of different MOFs.

**Figure. S17** Raman spectra of MOF substrates with and without the loading the of the R6G analyte.

**Figure. S18-19** Adsorption capacity and normalized EF values.

**Figure. S20-25** Energy-level diagrams of different MOFs.

**Figure. S26** SERS spectra of R6G ( $10^{-5}$  M) on the ZIF-67 substrate (tested in solution).

**Figure. S27** SERS signal intensities of R6G at varied concentrations on the ZIF-67 substrate.

**Figure. S28** Data for the evaluation of the limit of detection (LOD).

**Figure. S29** Schematic illustrating the GSCT process between analyte molecule and MOFs.

**Figure. S30-31** The stability and reproducibility of the MOFs substrate for SERS enhancement.

**Figure. S32** Schematic of the chemical bonding between silyloxy group and Co sites for the modification of ZIF-67 with APTES monomers.

**Figure. S33** SERS spectra for BPA on the APTES@ZIF-67 and bare Si/SiO<sub>2</sub> substrates.

**Figure S34.** Raman intensity-depth profile of the integrated intensity of  $520.6\text{ cm}^{-1}$  band for a Si wafer.

**Figure S35.** SERS spectra for PDAB on different MOF substrates.

**Figure. S36** Raman spectra of the Zn-TCPP substrate with and without the loading of R6G analyte.

**Figure. S37** SERS spectra of R6G on the Cu-TCPP substrate using 532 nm and 633 nm excitation laser.

**Figure. S38** The SERS spectra of R6G and MO at different excitation wavelengths (532 nm and 633 nm) on ZIF-67 and ZIF-8.

**Table S1** Elemental composition of APTES@ZIF-67 obtained by ICP-OES analysis.

<b>Supplementary Note S1.</b> Sampling approaches	S43
<b>Supplementary Note S2.</b> The confocal depth (h) of the laser beam	S44
<b>Supplementary Note S3.</b> Relationship between SERS signal intensity and R6G concentration	S45
<b>Supplementary Note S4.</b> Discussion about the SERS enhancement mechanism between Co-MOF-74 and Cu-TCPP MOFs	S46
<b>Supplementary Note S5.</b> Herzberg–Teller coupling term	S47
<b>Supplementary Note S6.</b> Discussion about the SERS enhancement mechanism between Co-MOF-74 and ZIF-8	S48
<b>Supplementary Note S7.</b> The role of charge-transfer transition in the selectivity and tailorability of MOF-based SERS substrate	S48
<b>Supplementary Note S8.</b> The advantage of MOFs-based substrates for surface modification	S49
<b>Supplementary Note S9.</b> The estimation of the detection limit for R6G	S50
<b>Supplementary Note S10.</b> The SERS effects of other toxic or important molecules	S51
<b>Supplementary Note S11.</b> The vibration band at about $1365\text{ cm}^{-1}$ of TCPP-based MOFs.	S52
<b>Supplementary Note S12.</b> The SERS performances of Cu-TCPP MOFs/R6G system at 633 nm laser excitation.	S52
<b>Supplementary Note S13.</b> The SERS performances of MOFs at two different excitation wavelengths (532 nm and 633 nm)	S54

<b>Supplementary Note S14.</b> Different types of resonances contributing to the SERS enhancement of MOFs	S55
<b>Supplementary Reference</b>	S56

## Experimental Section

**Materials.** Zinc nitrate hexahydrate ( $\text{Zn}(\text{NO}_3)_2 \cdot 6\text{H}_2\text{O}$ , 98%), Copper nitrate trihydrate ( $\text{Cu}(\text{NO}_3)_2 \cdot 3\text{H}_2\text{O}$ , 99%), Pyrazine (99%), Benzaldehyde(99.5%), Tetrakis(4-carboxyphenyl)porphyrin (TCPP, 97%), 2,5-Dihydroxyterephthalic acid(98%), (3-Aminopropyl)triethoxysilane were purchased from Aladdin. 2-methylimidazole (98%), Rhodamine 6G(95%) were purchased from Sigma-Aldrich. N,N-Dimethylformamide (DMF, 99.5%), Methanol (AR), Ethanol(AR), Methyl Orange(RG), Cobalt nitrate hexahydrate ( $\text{Co}(\text{NO}_3)_2 \cdot 6\text{H}_2\text{O}$ , 98.5%), phosphoric acid( $\text{H}_3\text{PO}_4$ , 85%) , toluene (99%) were purchased from Sinopharm Chemical Reagent Co., Ltd. All chemicals used were of high commercial purity and received without further purification.

**Characterizations.** The surface morphologies of the samples were measured using an FEI Quanta 400 FEG field emission scanning electron microscope (SEM). TEM images were obtained using an FEI Tecnai G2 F20 S-Twin at 200 kV. PXRD patterns of the samples were recorded on a Bruker AXS D8 Advance X-ray diffractometer with a  $\text{Cu K}\alpha$  radiation target (40V, 40A). UV-Vis spectra were collected in transmission geometry on a UV-Vis spectrophotometer (V660, JASCO) over a wavelength range of 200-800 nm. The properties of the pores in the MOF materials were analyzed from  $\text{N}_2$  adsorption-desorption isotherms obtained at 77 K using an adsorption apparatus (Micromeritics Tristar II3020M). The pore size distribution curves were calculated from the desorption branch of the nitrogen isotherm by the HK

(microporous region (<2 nm)) and BJH methods (mesoporous region (2-50 nm)). XPS measurements were performed on a PHI Quantera XPS scanning microprobe spectrometer with Al K $\alpha$  ( $h\nu = 1486.6$  eV) as the x-ray radiation source, which was carefully calibrated on the valence band.

**Preparation of ZIF-67.** Typically, Co(NO<sub>3</sub>)<sub>2</sub> 6H<sub>2</sub>O (1.64 g) was first dissolved in 80 mL of methanol. A mixture of 2-methylimidazole (3.70 g) with 80 mL methanol was then added to the above solution under vigorous stirring for 24 h. Finally, the purple product precipitates formed at the end of the reaction were collected by centrifugation, washed with methanol several times, and dried overnight at 60 °C. Before use, the samples were re-dried at 100 °C under vacuum for 5 h to remove the solvent.

**Preparation of ZIF-8.** Typically, Zn(NO<sub>3</sub>)<sub>2</sub> 6H<sub>2</sub>O (1.68 g) was first dissolved in 80 mL of methanol. A mixture of 2-methylimidazole (3.70 g) with 80 mL methanol was then added to the above solution under vigorous stirring for 24 h. Finally, the white product precipitates formed at the end of the reaction were collected by centrifugation, washed with methanol several times, and dried overnight at 60 °C. Before use, the samples were re-dried at 100 °C under vacuum for 5 h to remove the solvent<sup>1</sup>.

**Preparation of Co-TCPP MOFs.** Typically, Co(NO<sub>3</sub>)<sub>2</sub> 6H<sub>2</sub>O (8.7 mg, 0.03mmol), TCPP (7.9 mg, 0.01 mmol), pyrazine (1.6 mg, 0.02 mmol), DMF (1.5 mL) and ethanol (0.5 mL) were first mixed in a small capped vial, and then heated at 80 °C for

24 h. The dark red product precipitates formed at the end of the reaction were then collected by centrifugation, washed with ethanol several times, and re-dispersed in 2 mL of ethanol. Before use, the samples were re-dried at 60 °C to obtain a powder of Co-TCPP MOFs, and then re-dried at 100 °C under vacuum for 5 h to remove the solvent<sup>2</sup>.

**Preparation of Zn-TCPP MOFs.** Typically, Zn(NO<sub>3</sub>)<sub>2</sub> · 6H<sub>2</sub>O (8.9 mg, 0.03 mmol), TCPP (7.9 mg, 0.01 mmol), pyrazine (1.6 mg, 0.02 mmol), DMF (1.5 mL) and ethanol (0.5 mL) were first mixed in a small capped vial, and then heated at 80 °C for 24 h. The dark brown product precipitates formed at the end of the reaction were then collected by centrifugation, washed with ethanol several times, and re-dispersed in 2 mL of ethanol. Before use, the samples were re-dried at 60 °C to obtain a powder of Zn-TCPP MOFs, and then re-dried at 100 °C under vacuum for 5 h to remove the solvent<sup>2</sup>.

**Preparation of Cu-TCPP MOFs.** Typically, Cu(NO<sub>3</sub>)<sub>2</sub> · 3H<sub>2</sub>O (21.6 mg, 0.09 mmol), TCPP (23.7 mg, 0.03 mmol), DMF (1.5 mL) and ethanol (0.5 mL) were first mixed in a small capped vial, and then heated at 80 °C for 24 h. The red product precipitates formed at the end of the reaction were then collected by centrifugation, washed with ethanol several times, and re-dispersed in 2 mL of ethanol. Before use, the samples were re-dried at 60 °C to obtain a powder of Cu-TCPP MOFs, and then re-dried at 100 °C under vacuum for 5 h to remove the solvent<sup>2</sup>.

**Preparation of Co-MOF-74.** Typically, 2,5-dihydroxyterephthalic acid (144.4 mg, 0.729 mmol) and  $\text{Co}(\text{NO}_3)_2 \cdot 6\text{H}_2\text{O}$  (713 mg, 2.45 mmol) were first dissolved in a mixture of DMF-ethanol-water (1:1:1 volume ratio, 60 mL) under vigorous stirring for 1 h, and then heated at 100 °C for 24 h. The red-orange product precipitates formed at the end of the reaction were then collected by centrifugation, washed with methanol several times, and dried overnight at 60 °C. Before use, the samples were re-dried at 100 °C under vacuum for 5 h to remove the solvent<sup>3</sup>.

**Acid etching of ZIF-67.** The as-prepared ZIF-67 samples were put into a phosphoric acid/DMF solution (1:479 volume ratio), and sonicated for 10 minutes at room temperature. The samples were kept at 60 °C in an oven for 2 hours to control the extent of the etching. After the acid etching was completed, the etched samples were washed with DMF and ethanol several times, and dried under vacuum overnight<sup>4</sup>.

**Preparation of APTES@ZIF-67.** Before surface modification, the original ZIF-67 sample was dried at 100 °C under vacuum for 5 h to remove the solvent. The sample was then immersed in a solution containing 30 ml of anhydrous toluene and 1.5 ml of (3-aminopropyl)triethoxysilane and subsequently refluxed at 110 °C for 20 hours. Finally, the surface-modified ZIF-67 sample was washed with hexane to remove the excess unreacted reagents, and dried under vacuum overnight.

**Raman measurement.** The SRES behaviors of these MOF materials were examined using R6G as a target molecule at an excitation wavelength of 532 nm. Typically, a stock solution of  $10^{-3}$  M R6G was initially prepared, which was diluted to form R6G aqueous solutions with concentrations ranging from  $10^{-4}$  to  $10^{-7}$  M. Next, 800  $\mu$ L R6G solutions with known concentrations were mixed with 200  $\mu$ L of MOFs aqueous solution (0.3 mg/ml) and then stored in the dark for 2 hours to reach the adsorption-desorption equilibrium. Finally, 20  $\mu$ L of suspension was dripped onto a cleaned silicon wafer before drying at 60  $^{\circ}$ C for 2 hours.

Raman spectra were subsequently achieved on a high-resolution confocal Raman spectrometer (LabRAM HR-800). A 50  $\times$  L objective lens with a laser spot diameter of about 1  $\mu$ m and power of 0.3 mW in all acquisitions was used to collect the Raman spectra, with an acquisition time of 5 s. Raman spectra from different locations were collected for each sample, with the signal intensity averaged for final analysis to estimate the RSD values of the enhancement factors. Using a similar procedure, the SRES behaviors of these MOF materials were also examined using MO as a target molecule at an excitation wavelength of 633 nm.

The SERS behaviors of ZIF-67 and APTES@ZIF-67 were examined using benzaldehyde as a target molecule at an excitation wavelength of 532 nm. Typically, 3 ml of MOF substrate dispersed in ethanol (0.1 mg/ml) was mixed with different volumes of benzaldehyde (50, 40, 30, 20, and 10  $\mu$ L, respectively). The solutions were then stored in the dark for 2 hours to reach the adsorption-desorption equilibrium. Finally, 20  $\mu$ L of the suspension was dripped onto a clean silicon wafer

before drying at room temperature for 2 hours. The Raman test conditions were the same as that described above.

**Calculation of the enhancement factor:** The  $EF$  was calculated according to the formula:

$$EF=(I_{\text{SERS}}/N_{\text{SERS}})/(I_{\text{bulk}}/N_{\text{bulk}}) \quad (1)$$

$$N_{\text{SERS}}=CVN_{\text{A}}A_{\text{Raman}}/A_{\text{Sub}} \quad (2)$$

$$N_{\text{bulk}}=\rho hA_{\text{Raman}}N_{\text{A}}/M \quad (3)$$

where  $I_{\text{SERS}}$  and  $I_{\text{bulk}}$  are the intensities of the selected Raman peak in the SERS and normal Raman spectra, and  $N_{\text{SERS}}$  and  $N_{\text{bulk}}$  are the average number of molecules in the scattering area on the SERS and non-SERS substrates, respectively. The data of R6G (0.05 M) on the non-SERS Si/SiO<sub>2</sub> wafer were used as the normal Raman reference. Specifically, the intensity was averaged from the data on 20 random spots, and the number of analyte molecules within the scattering area was estimated by Supplementary equation 2 on the assumption of a uniform distribution of the analyte molecules on the substrates.  $C$  is the molar concentration of the analyte solution,  $V$  is the volume of the droplet, and  $N_{\text{A}}$  is the Avogadro constant.  $A_{\text{Raman}}$  is the laser spot area (1  $\mu\text{m}$  in diameter) of the Raman scanning. 20  $\mu\text{L}$  of the analyte solution on substrate spread spontaneously into a circle of about 3 mm in diameter after the solvent evaporated. The effective area of the substrate  $A_{\text{Sub}}$  can then be obtained. For bulk R6G with a molecular weight ( $M$ ) of 479 g/mol and density ( $\rho$ ) of 1.15 g  $\cdot$  cm<sup>-3</sup>, the confocal depth ( $h$ ) of the laser beam is 23.64  $\mu\text{m}$ , and  $N_{\text{bulk}}$  can be calculated by

Supplementary equation 3<sup>5-6</sup>.

**Adsorption capacity measurement:** 800  $\mu\text{L}$  of R6G solution ( $10^{-5}$  M) was mixed with 200  $\mu\text{L}$  of MOFs aqueous solution (0.3 mg/ml), followed by storing in the dark for 2 hours to reach the adsorption-desorption equilibrium. The R6G left in solution was collected by centrifugation with the absorbance subsequently measured by UV-Vis absorption spectroscopy. Finally, the amount of un-adsorbed R6G was calculated according to Lambert-Beer law:  $A=Kbc$ .

**The reproducibility and stability for statistical analysis: For the estimation of the reproducibility of MOF substrates.** 20 spectra from four different substrates (five stochastic spots per substrate) are acquired to estimate the reproducibility of the different substrates. Intensities of the  $612\text{ cm}^{-1}$  ( $P_1$ ) band for the R6G Raman spectrum and  $1115\text{ cm}^{-1}$  ( $P_5$ )<sup>7</sup> band for the MO Raman spectrum are chosen for quantification. For the examination of the stability of MOF substrates, Raman profiles of R6G ( $10^{-5}$  M) acquired from MOF substrates after two days of storage in the open air are compared with those obtained on freshly prepared ones.

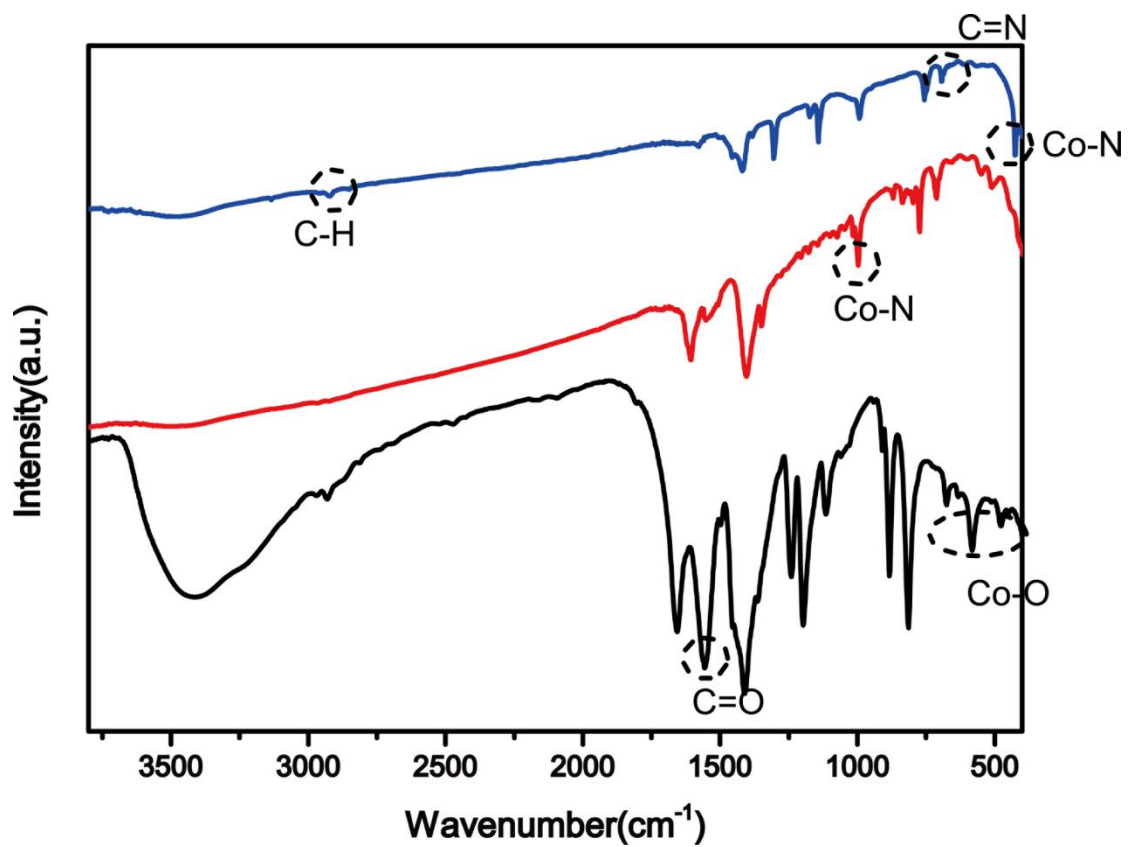


**Figure. S1** FTIR spectra of ZIF-67, Co-TCPP MOFs and Co-MOF-74.

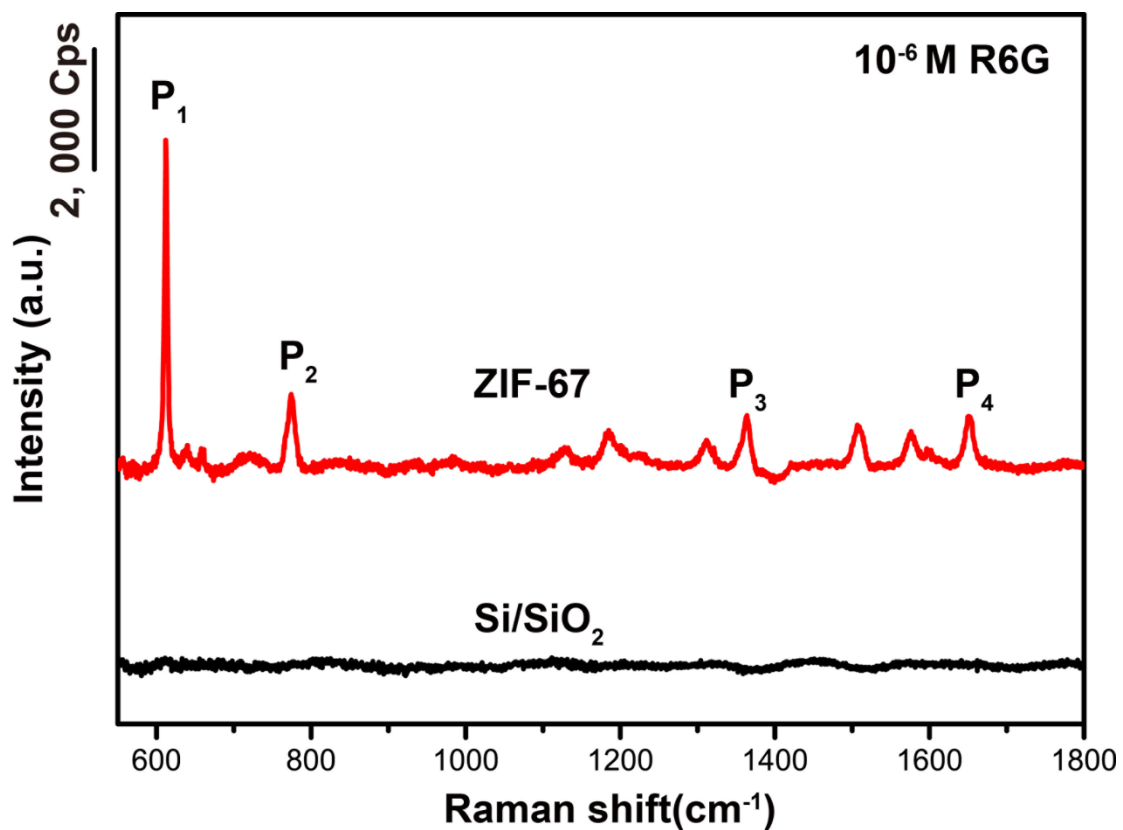


**Figure. S2** SERS spectra for R6G ( $10^{-6}$  M) on the ZIF-67 and Si/SiO<sub>2</sub> substrates. Almost no clear signals related to the R6G molecule can be discerned on the bare SiO<sub>2</sub>/Si substrate except for the fluorescence background, while a substantial Raman enhancement for R6G is observed on the ZIF-67 substrate.

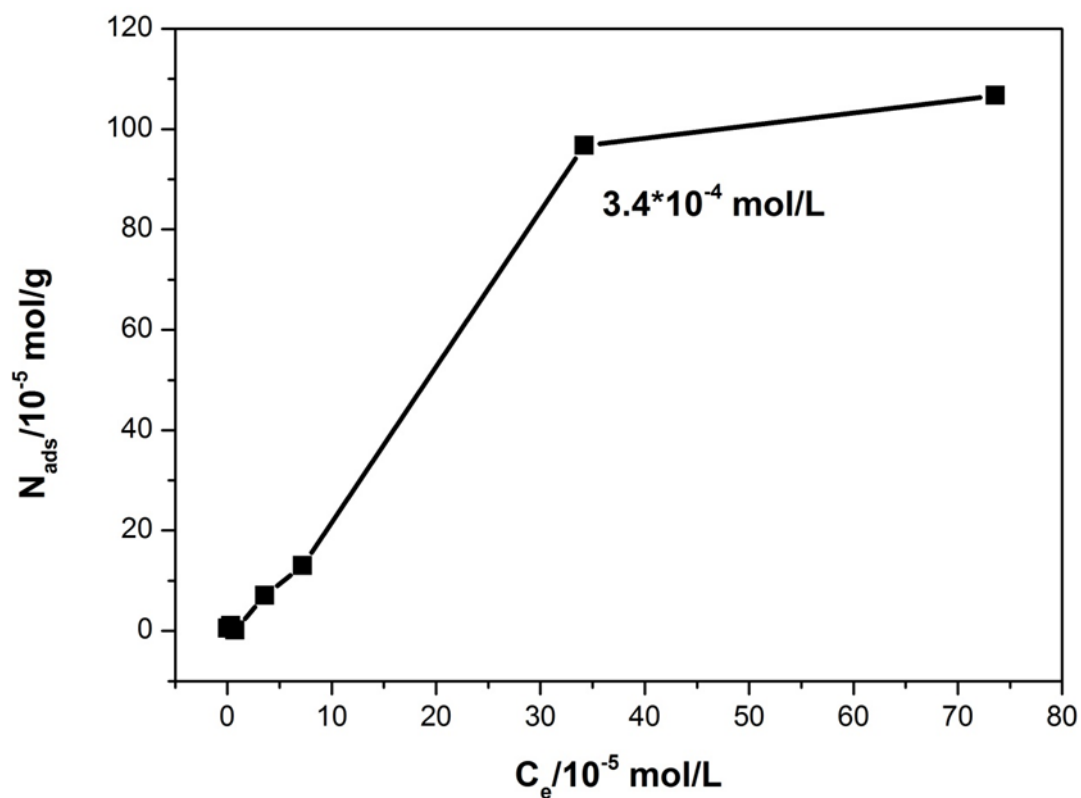


**Figure. S3** R6G adsorption isotherm shows a plot of the adsorbed amount versus the equilibrium concentration of R6G on the as-prepared ZIF-67 substrate. For an initial concentration of R6G less than  $3.4 \times 10^{-4} \text{ M}$ , the maximum amount of R6G absorbed onto the ZIF-67 substrate (the effective substance concentration of ZIF-67 is about  $0.06 \text{ mg/ml}$ ) is not reached.

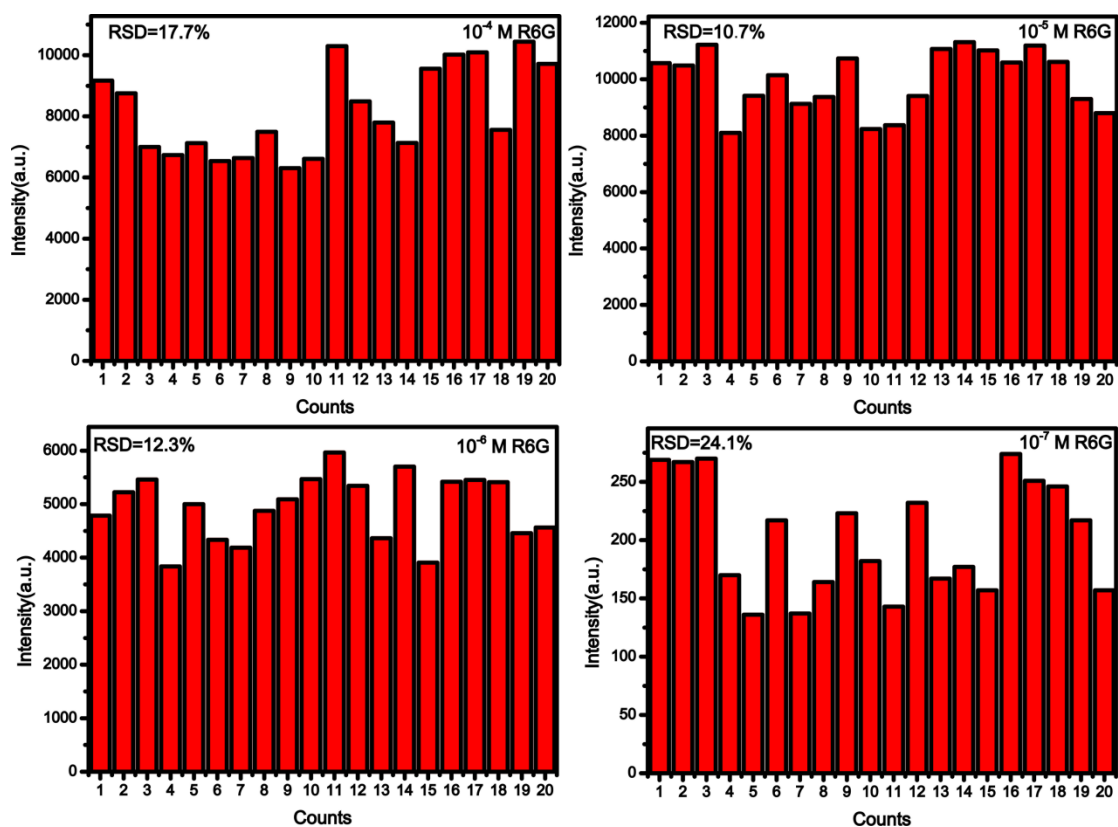


**Figure. S4** The intensities of the  $P_1$  ( $612\text{ cm}^{-1}$ ) Raman vibration mode of R6G on the different ZIF-67 substrates. Four different concentrations of R6G, namely  $10^{-4}$ ,  $10^{-5}$ ,  $10^{-6}$ , and  $10^{-7}$  M, are examined using data acquired by recording 20 spectra from four different substrates. The RSDs of the  $P_1$  mode of R6G at the four different concentrations,  $10^{-4}$ ,  $10^{-5}$ ,  $10^{-6}$ , and  $10^{-7}$  M, are calculated to be 17.7%, 10.7%, 12.3%, and 24.1%, respectively.

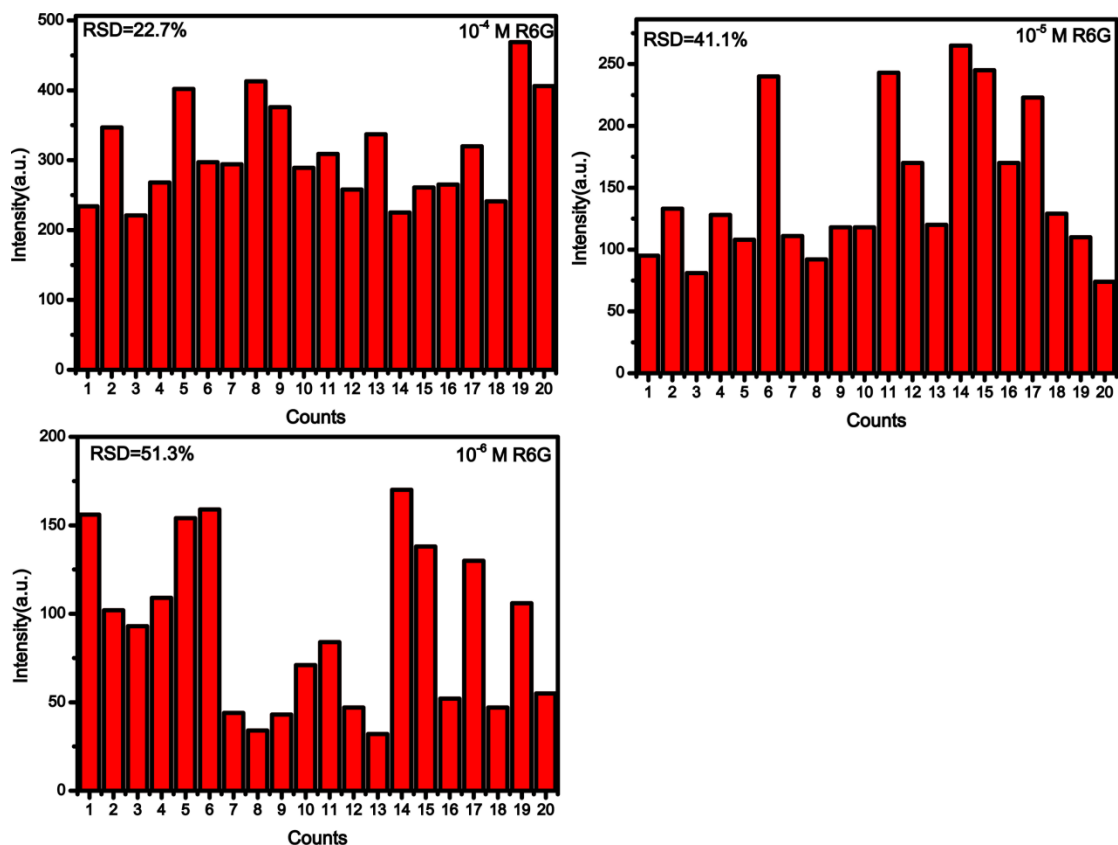


**Figure. S5** The intensities of the P<sub>1</sub> (612 cm<sup>-1</sup>) Raman vibration mode of R6G on the different Co-TCPP substrates. Three different concentrations of R6G, namely 10<sup>-4</sup>, 10<sup>-5</sup>, and 10<sup>-6</sup> M, are examined using data acquired by recording 20 spectra from three different substrates. The RSDs of the P<sub>1</sub> mode of R6G at the three different concentrations, 10<sup>-4</sup>, 10<sup>-5</sup> and 10<sup>-6</sup> M, are calculated to be 22.7%, 41.1%, and 51.3%, respectively.

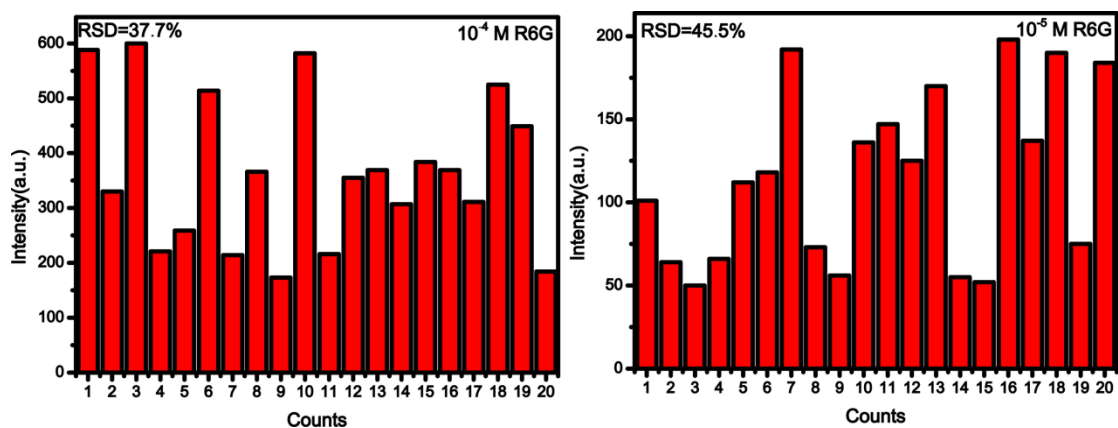


**Figure. S6** The intensities of the P<sub>1</sub> (612 cm<sup>-1</sup>) Raman vibration mode of R6G on different Co-MOF-74 substrates. Two different concentrations of R6G 10<sup>-4</sup> and 10<sup>-5</sup> M are examined using data acquired by recording 20 spectra from two different substrates. The RSDs of the P<sub>1</sub> mode of R6G at the two different concentrations, 10<sup>-4</sup> and 10<sup>-5</sup> M, are calculated to be 37.7% and 45.5%, respectively.

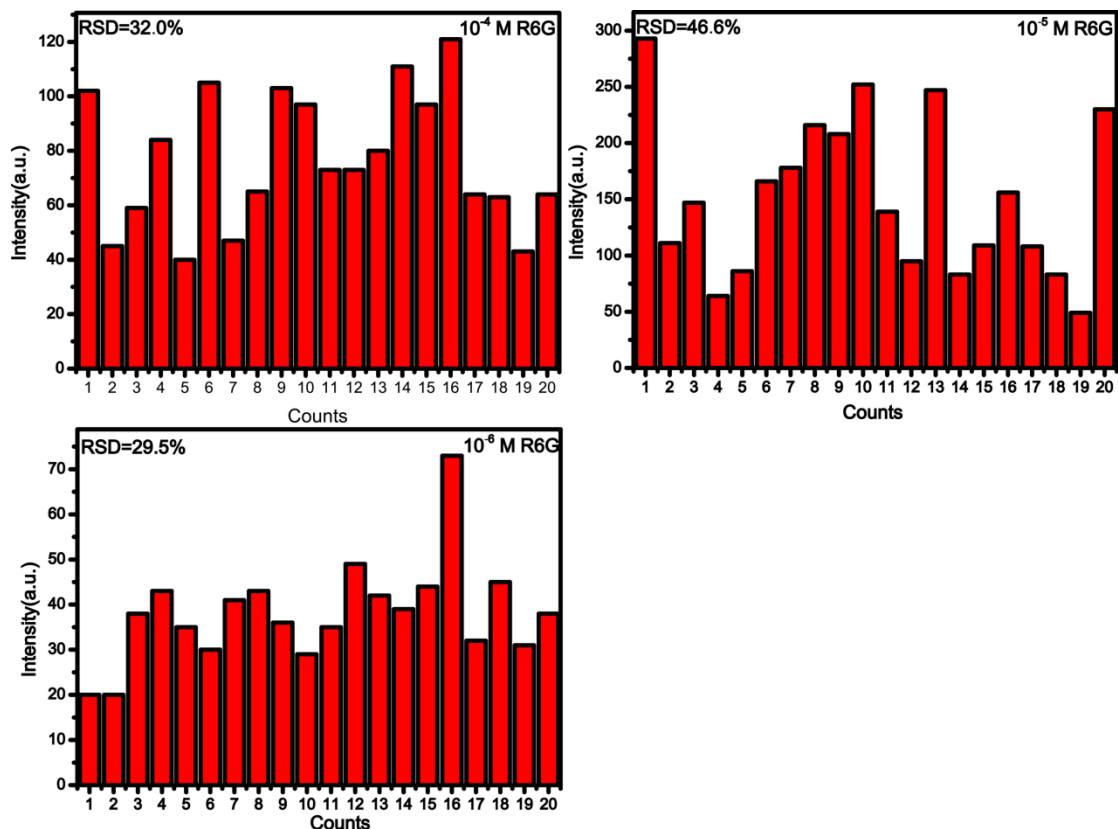


**Figure. S7** The intensities of the P<sub>1</sub> (612 cm<sup>-1</sup>) Raman vibration mode of R6G on the

different Cu-TCPP substrates. Three different concentrations of R6G,  $10^{-4}$ ,  $10^{-5}$ , and  $10^{-6}$  M, are examined using data acquired by recording 20 spectra from three different substrates. The RSDs of the  $P_1$  mode of R6G at the three different concentrations,  $10^{-4}$ ,  $10^{-5}$ , and  $10^{-6}$  M, are calculated to be 32.0%, 46.6%, and 29.5%, respectively.

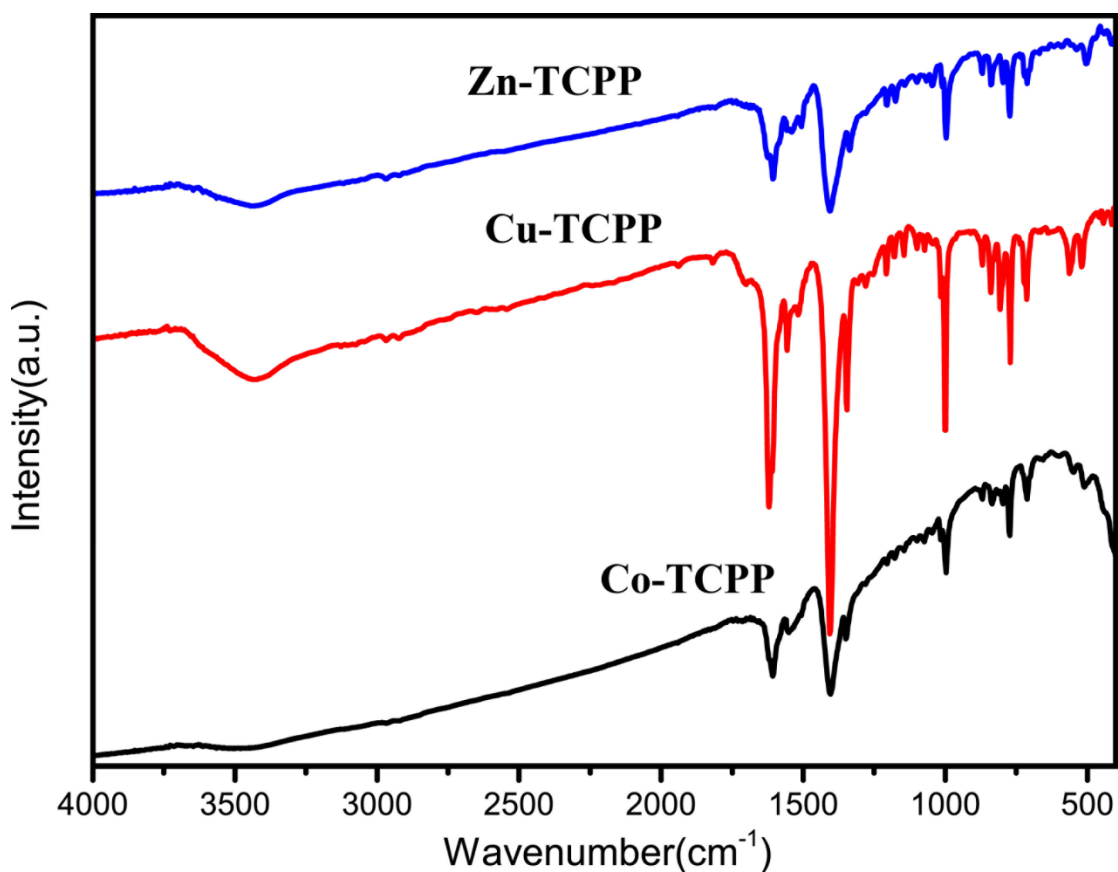


**Figure. S8** FTIR spectra of the Co-TCPP MOFs, Cu-TCPP MOFs, and Zn-TCPP MOFs.

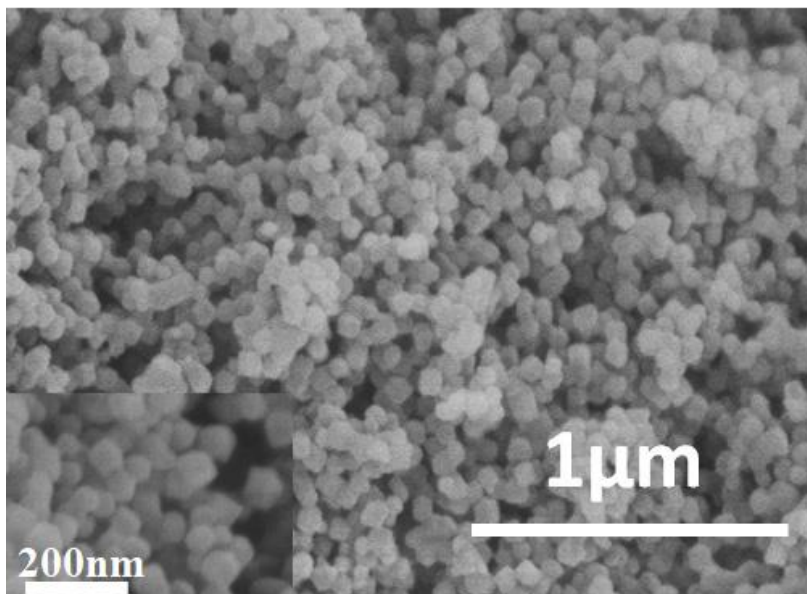


**Figure. S9** SEM image of the ZIF-8 crystals.

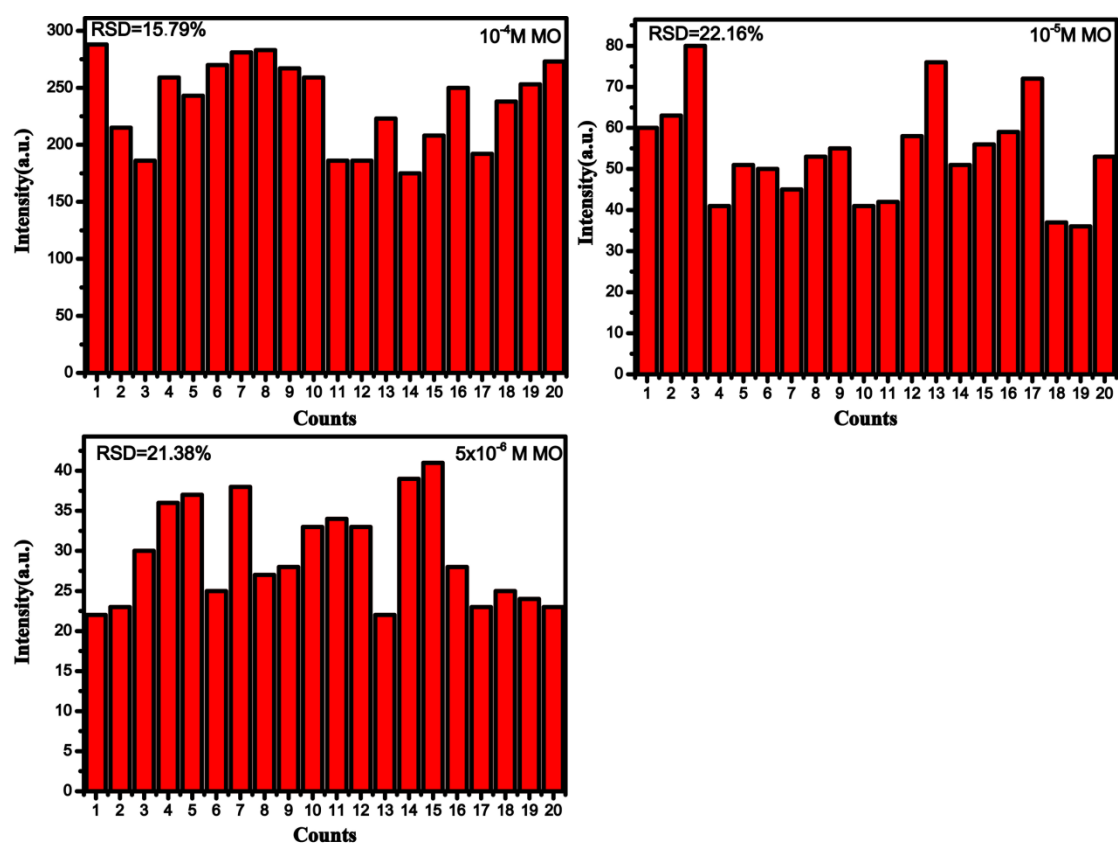


**Figure. S10** The intensities of the P<sub>5</sub> (1115 cm<sup>-1</sup>) Raman vibration mode of MO on different ZIF-8 substrates. Three different concentrations of MO, 10<sup>-4</sup>, 10<sup>-5</sup>, and 5 ×

$10^{-6}$  M, are examined using data acquired by recording 20 spectra from three different substrates. The RSDs of the  $P_5$  mode of MO at three different concentrations,  $10^{-4}$ ,  $10^{-5}$ , and  $5 \times 10^{-6}$  M, are calculated to be 15.7%, 22.1%, and 21.3%, respectively.

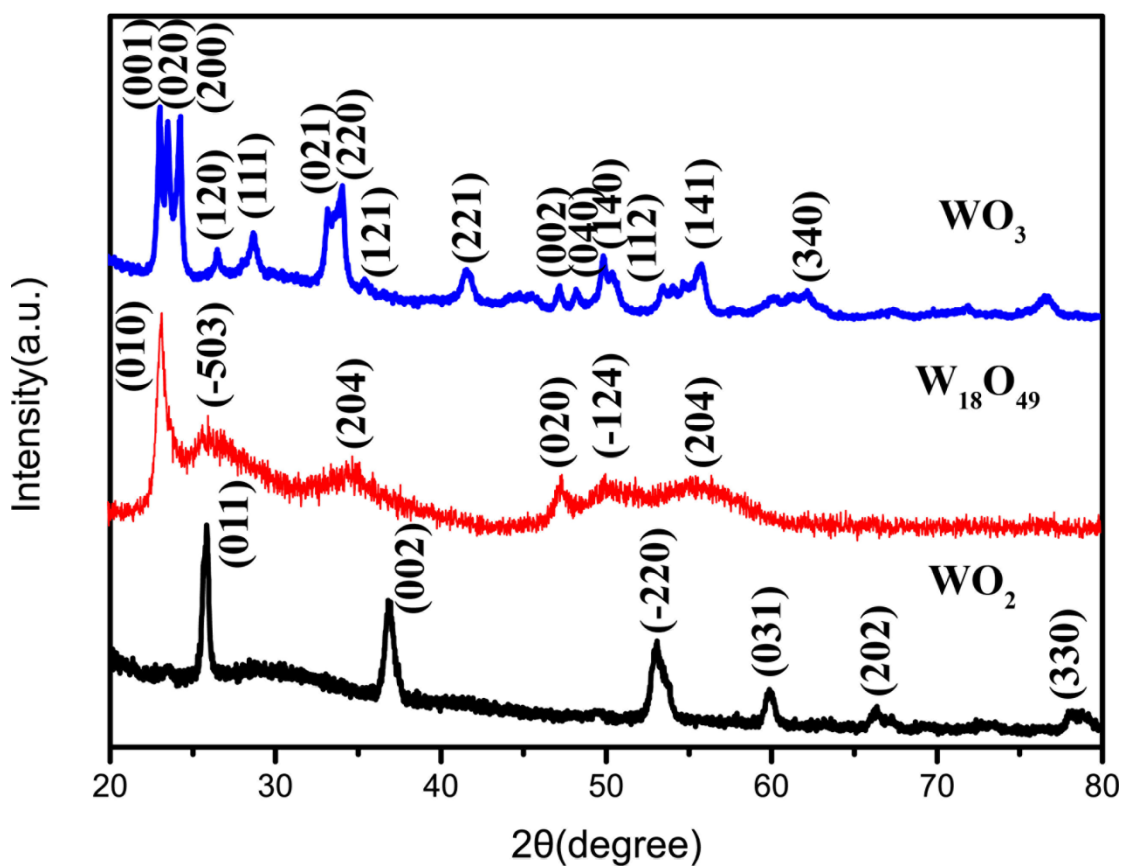


**Figure. S11** PXRD patterns of  $\text{WO}_3$ ,  $\text{W}_{18}\text{O}_{49}$ , and  $\text{WO}_2$  samples.

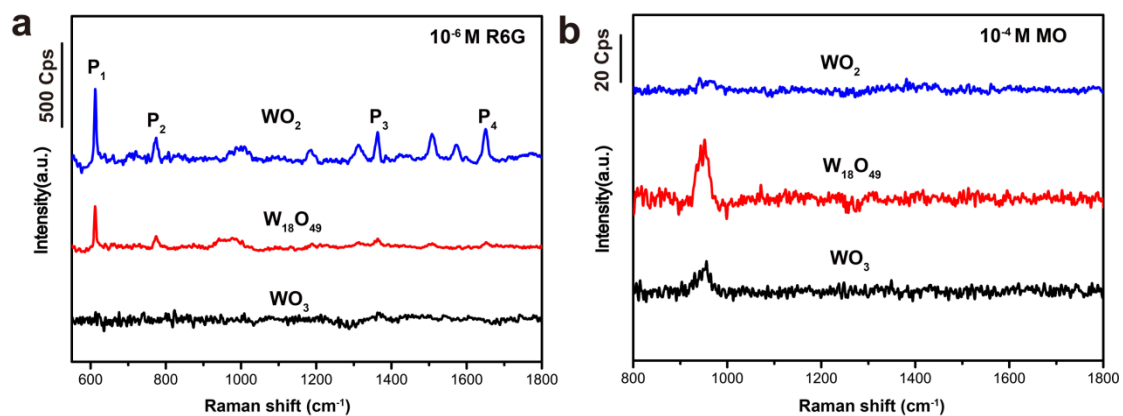


**Figure. S12** (a) SERS spectra of R6G ( $10^{-6}$  M) on the  $\text{WO}_2$ ,  $\text{W}_{18}\text{O}_{49}$ , and  $\text{WO}_3$

substrates when excited by a 532 nm laser. (b) SERS spectra of MO ( $10^{-4}$  M) on the  $\text{WO}_2$ ,  $\text{W}_{18}\text{O}_{49}$ , and  $\text{WO}_3$  substrates when excited by a 633 nm laser.

To demonstrate the unique tailorability of MOFs as SERS substrates, the selective detection of two different target molecules (R6G and MO) using semiconductor materials as SERS substrates are examined to provide a comparison. Tungsten oxide, characterized by its tremendous sub-stoichiometric compositions, is taken as an example due to the greater flexibility of its electronic structures over most other semiconductors. Three types of tungsten oxide samples with different concentrations of oxygen vacancies,  $\text{WO}_3$ ,  $\text{W}_{18}\text{O}_{49}$ , and  $\text{WO}_2$ , are prepared as SERS substrates, with their phase structures well-confirmed by the PXRD measurements (Figure S11). It can be observed that all three substrates show distinct SERS enhancement for R6G detection ( $10^{-6}$  M) under 532 nm laser excitation. Notably, the SERS intensity is shown to increase with the increase of the oxygen vacancy concentration in the tungsten oxide,  $\text{WO}_3 < \text{W}_{18}\text{O}_{49} < \text{WO}_2$  (Figure S12a). However, for the detection of MO ( $10^{-4}$  M), almost no SERS signals belonging to the target molecules are detected on all three substrates (Figure S12b), probably due to the lack of thermodynamically-feasible resonances such as exciton, charge-transfer, and molecule resonances, which cannot be manipulated to be in resonance with the incident laser frequency (633 nm) due to the limited flexibility of the band structures of semiconductors. This contrastive result clearly highlights that MOFs as SERS substrates with high tailorability provide excellent selectivity for different target molecules.

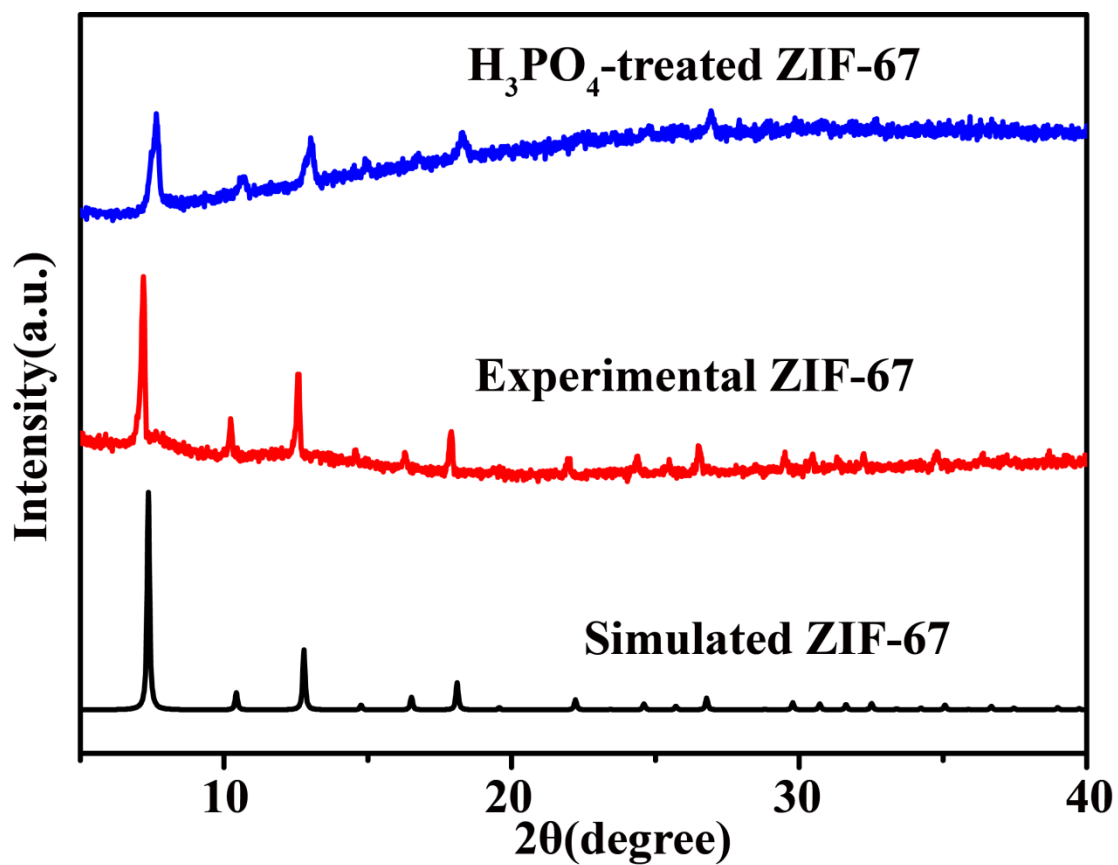


**Figure. S13** PXRD patterns of ZIF-67, acid-treated ZIF-67, and simulated ZIF-67 crystals, respectively.

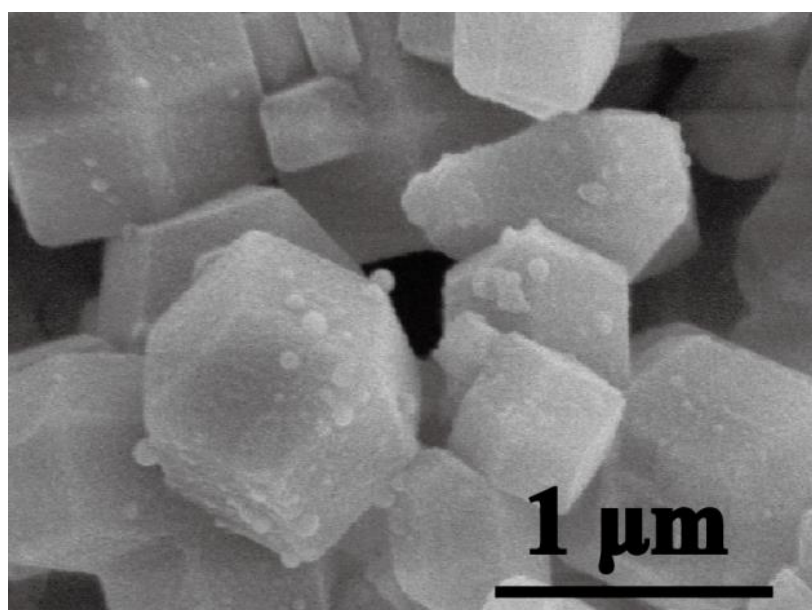


**Figure. S14** SEM image of APTES@ZIF-67 crystals.

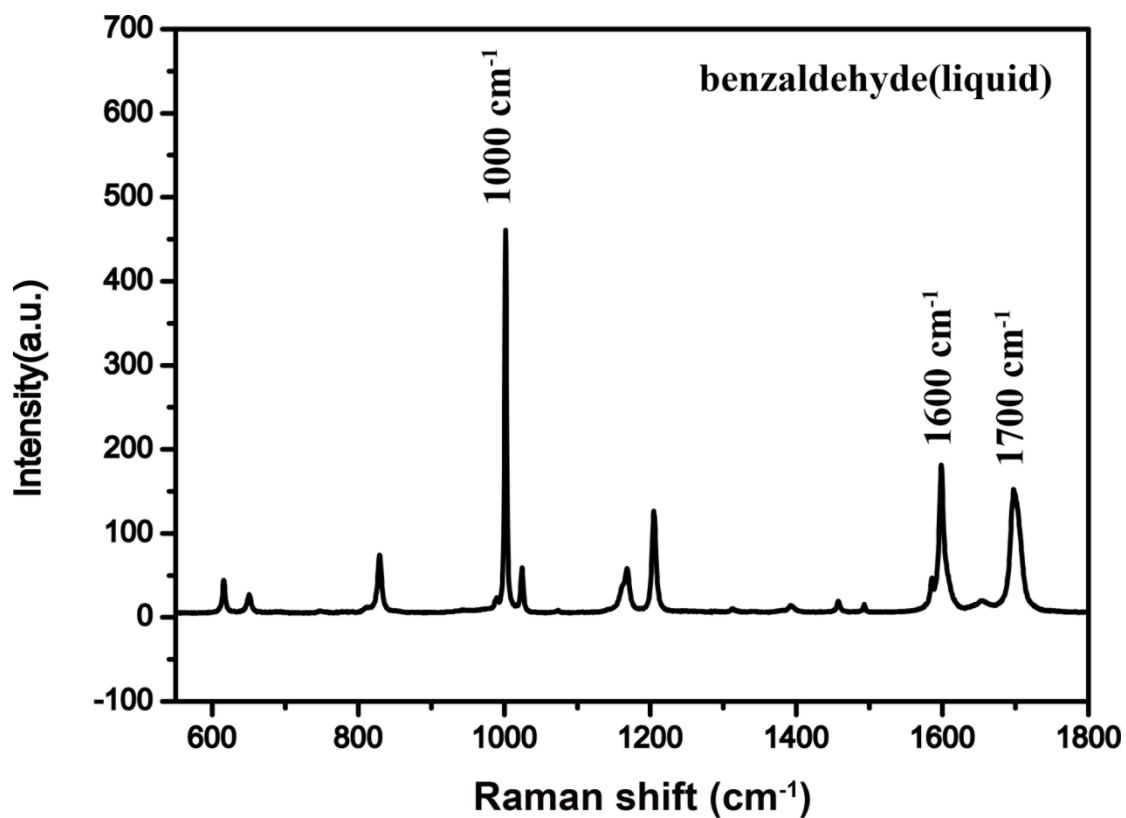
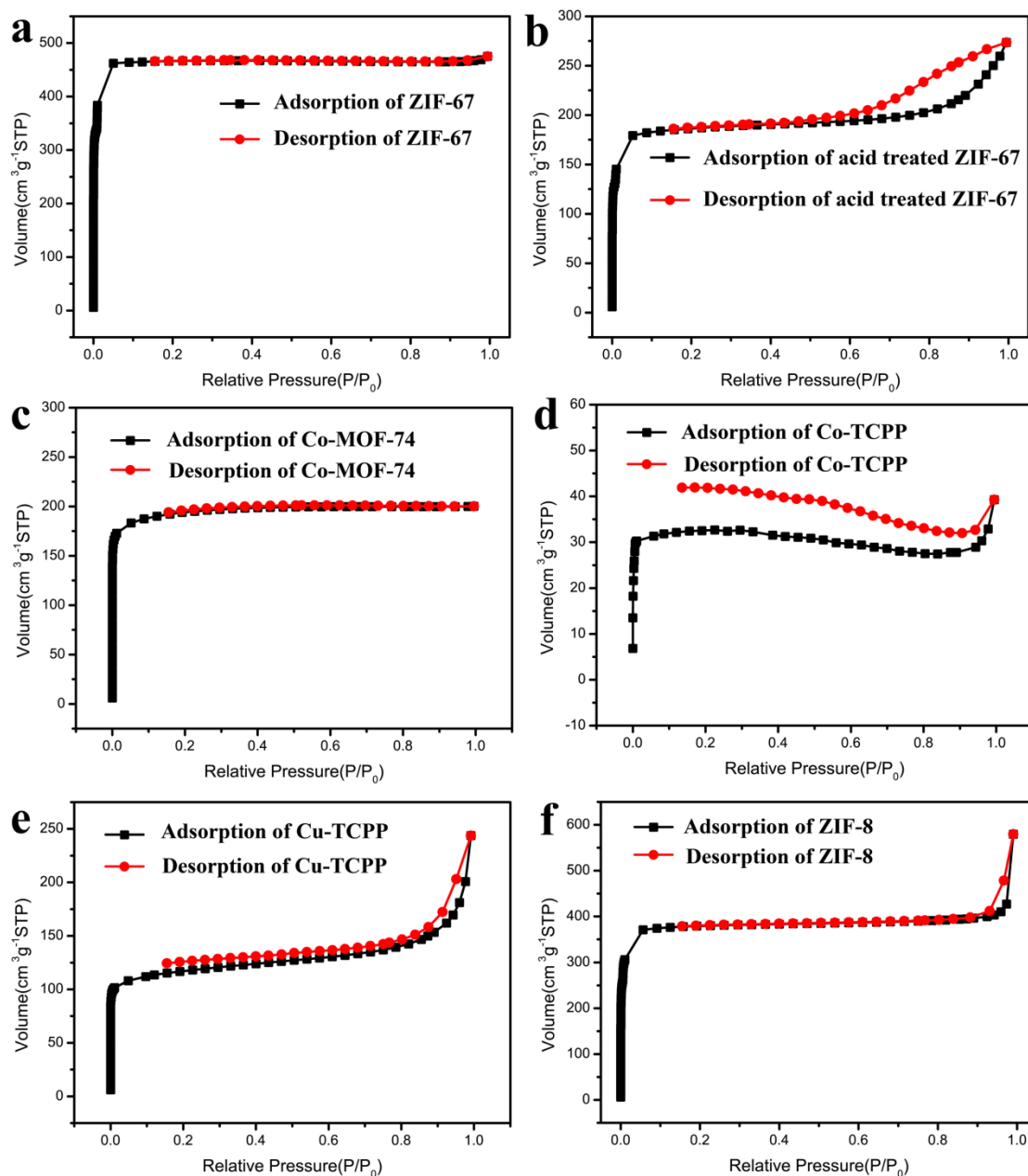
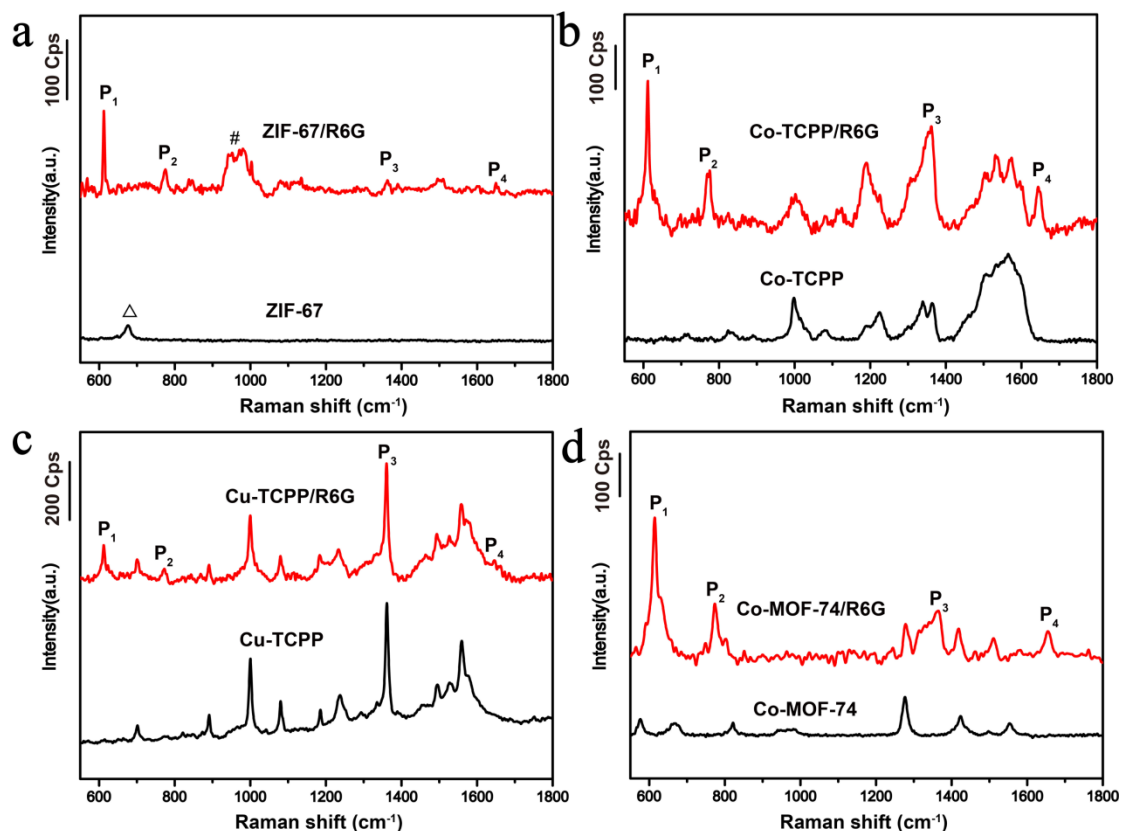


Figure. S15 Raman spectrum of liquid-phase benzaldehyde.



**Figure. S16**  $N_2$  adsorption-desorption isotherms of (a-b) the raw and acid-treated ZIF-67 samples, (c) Co-MOF-74, (d) Co-TCPP MOFs, (e) Cu-TCPP MOFs, and (f) ZIF-8.



**Figure. S17** Raman spectra of MOF substrates with and without the loading of the R6G analyte, for (a) ZIF-67, (b) Co-TCPP MOFs, (c) Cu-TCPP MOFs, and (d) Co-MOF-74. The characteristic band of ZIF-67 centered at  $677\text{ cm}^{-1}$  is denoted as “ $\Delta$ ”, and the band labeled as “#” is likely to be attributed to the Si-H bonds on the surface of Si/SiO<sub>2</sub><sup>8</sup>. Also note that the characteristic band of the Co-TCPP MOFs and Cu-TCPP MOFs centered at  $1360\text{ cm}^{-1}$  shows appreciable overlapping with the P<sub>3</sub> band of the R6G analyte.

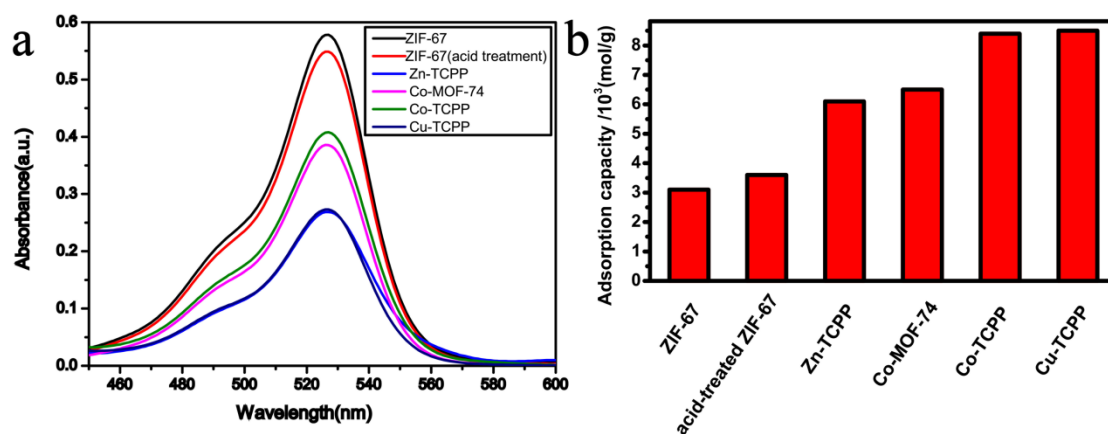


**Figure. S18** (a) Absorption spectra for R6G left in the solution at adsorption-desorption equilibrium in the presence of ZIF-67, acid-treated ZIF-67, Zn-TCPP, Co-MOF-74, Co-TCPP, and Cu-TCPP substrates, respectively. (b) Adsorption capacities of ZIF-67, acid-treated ZIF-67, Zn-TCPP, Co-MOF-74, Co-TCPP, and Cu-TCPP substrates determined from the decrease in the dye concentrations. The smallest adsorption capacity shown by ZIF-67 may be ascribed to its small pore size (0.76 nm), incapable for the accommodation of R6G molecule in a dimension of about  $0.8 \text{ nm} \times 1.6 \text{ nm}$ . Instead, for TCPP-based MOFs and Co-MOF-74 with an average pore size of 1.18 nm and  $1.2 \text{ nm}^{2,9}$ , the R6G molecule may enter into the pores of the MOFs along the long axis for an enhanced adsorption capacity.

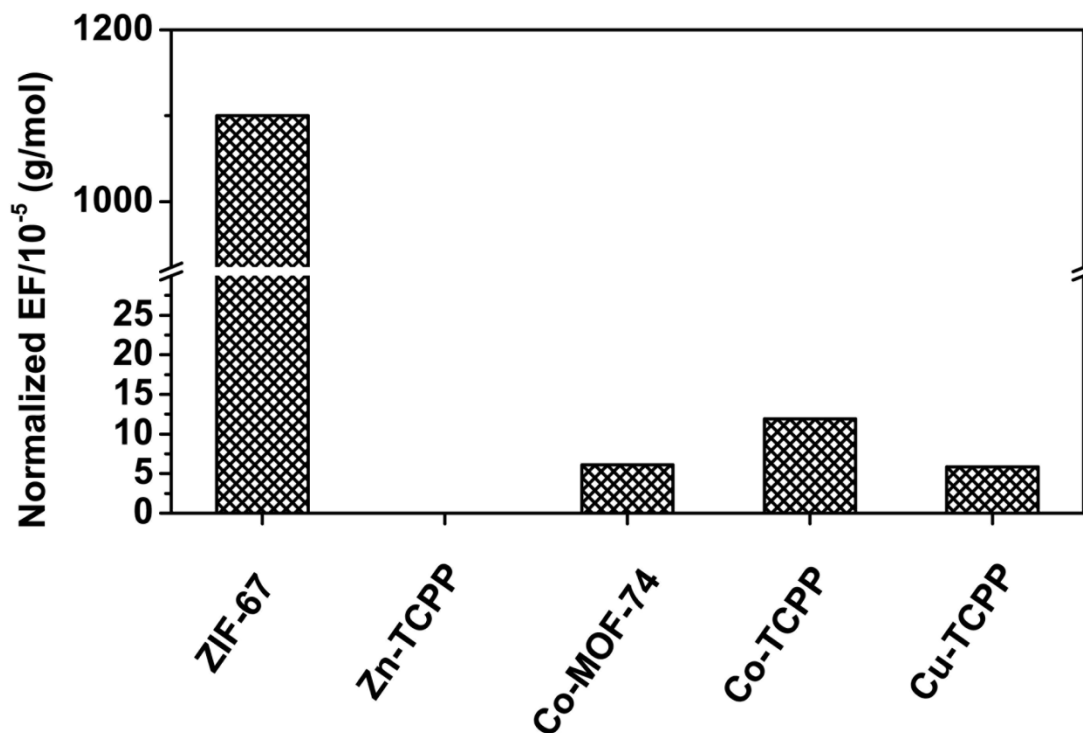


**Figure. S19** A summary comparison of the EF values of ZIF-67, Zn-TCPP, Co-MOF-74, Co-TCPP, and Cu-TCPP substrates, which is normalized by the adsorption capacity of R6G. The result shows that although ZIF-67 has the lowest adsorption capacity, it exhibits the best SERS enhancement among the measured SERS substrates.

Here, the adsorption capacity and adsorption orientation of R6G molecules on MOF substrate are excluded as the main reason for the considerable difference in the SERS behavior over different MOF materials. Firstly, the adsorption capacity toward R6G analyte is taken into consideration from the aspect of the nano-scaled cavities in MOFs (Figure S18). Interestingly, the most significant SERS enhancement is obtained on a substrate with lowest R6G adsorption, that is, ZIF-67 substrate shows the largest normalized EF value for R6G detection (Figure S19), which suggests that the adsorption capacity toward analyte is not the main reason for the observed SERS

enhancement on MOF substrates. Secondly, adsorption orientation of analyte on MOF substrates is examined from the aspect of the variation of ligand groups on MOFs, by a comparison between intensities of the three characteristic vibration modes  $P_1$ ,  $P_2$ , and  $P_4$  (Figures 1f and 2f). Clearly,  $P_1$  band is most enhanced among three characteristic peaks on all the MOF substrates except the non-SERS active Zn-TCPP substrates, whereas  $P_4$  band is only weakly enhanced, which indicates that the aromatic rings of R6G are either not parallel to the aromatic rings of MOF substrates or are separated from the aromatic rings of MOF substrates by chemical groups<sup>10</sup>. Thus, the adsorption orientation also doesn't play an important role in MOFs-mediated SERS enhancement.

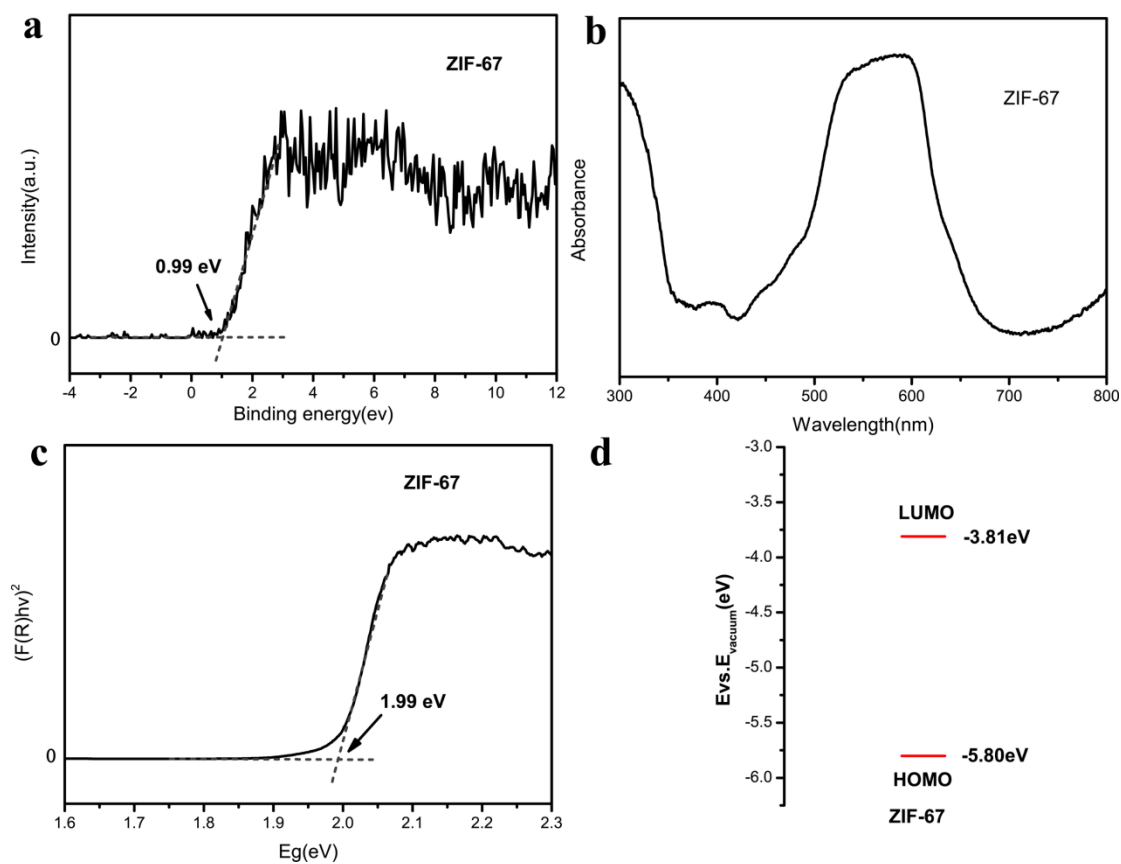


**Figure. S20** (a) Valence-band XPS spectrum of ZIF-67. The HOMO position of the ZIF-67 sample is determined by linear extrapolation of the leading edges of the profile to the base line<sup>11-12</sup>. After calibration with the reference Fermi level, the HOMO value for ZIF-67 is calculated to be 5.80 eV with respect to vacuum. (b) UV-Vis absorption spectrum and (c) a plot of the transformed Kubelka-Munk function versus the energy of the exciting light, giving a band-gap energy of 1.99 eV for ZIF-67, which is in accordance with the literature<sup>13</sup>. (d) Energy-level diagram of ZIF-67. Based on the energy values of the HOMO level and band-gap, the LUMO level of ZIF-67 is determined to be about -3.81 eV with respect to vacuum.

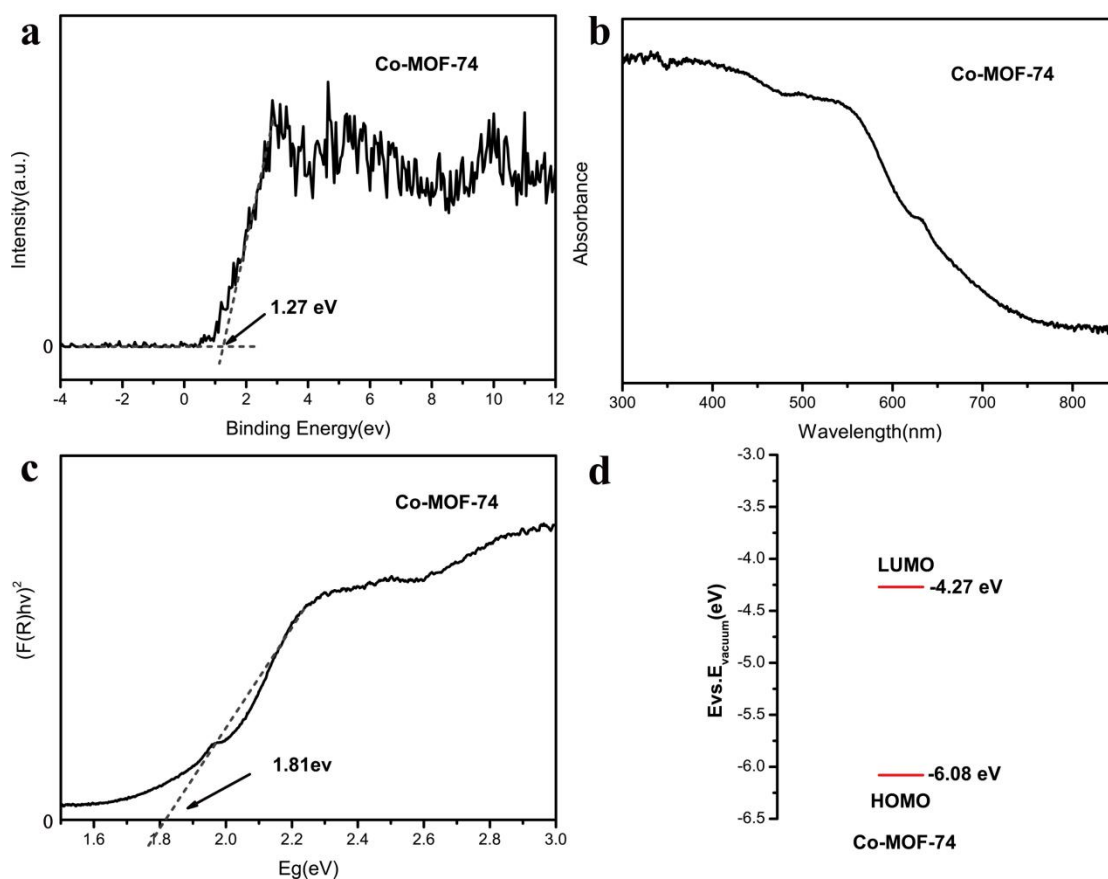


**Figure. S21** (a) Valence-band XPS spectrum of Co-MOF-74. The HOMO position of Co-MOF-74 is determined by linear extrapolation of the leading edges of the profile to the base line<sup>11-12</sup>. After calibration with the reference Fermi level, the HOMO value for Co-MOF-74 is calculated to be 6.08 eV with respect to vacuum. (b) UV-Vis absorption spectrum and (c) a plot of the transformed Kubelka-Munk function versus the energy of the exciting light, giving a band-gap energy of 1.81 eV for Co-MOF-74. (d) Energy-level diagram of Co-MOF-74. Based on the energy values of the HOMO level and band-gap, the LUMO level of Co-MOF-74 is determined to be about -4.27 eV with respect to vacuum.

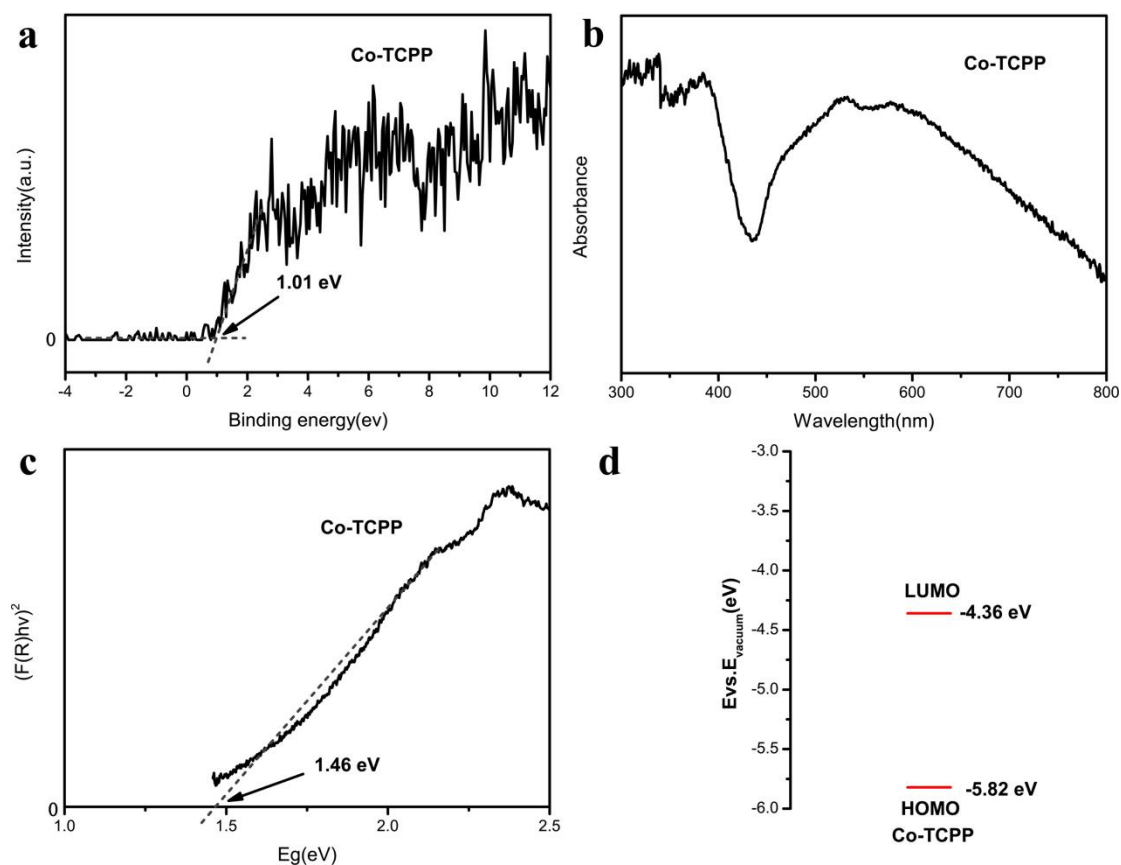


**Figure. S22** (a) Valence-band XPS spectrum of Co-TCPP MOFs. The HOMO position of Co-TCPP MOFs is determined by linear extrapolation of the leading edges of the profile to the base line<sup>11-12</sup>. After calibration with the reference Fermi level, the HOMO value for Co-TCPP MOFs is calculated to be 5.82 eV with respect to vacuum. (b) UV-Vis absorption spectrum and (c) a plot of the transformed Kubelka-Munk function versus the energy of the exciting light, giving a band-gap energy of 1.46 eV for Co-TCPP MOFs. (d) Energy-level diagram of Co-TCPP MOFs. Based on the energy values of the HOMO level and band-gap, the LUMO level of Co-TCPP MOFs is determined to be about -4.36 eV with respect to vacuum.

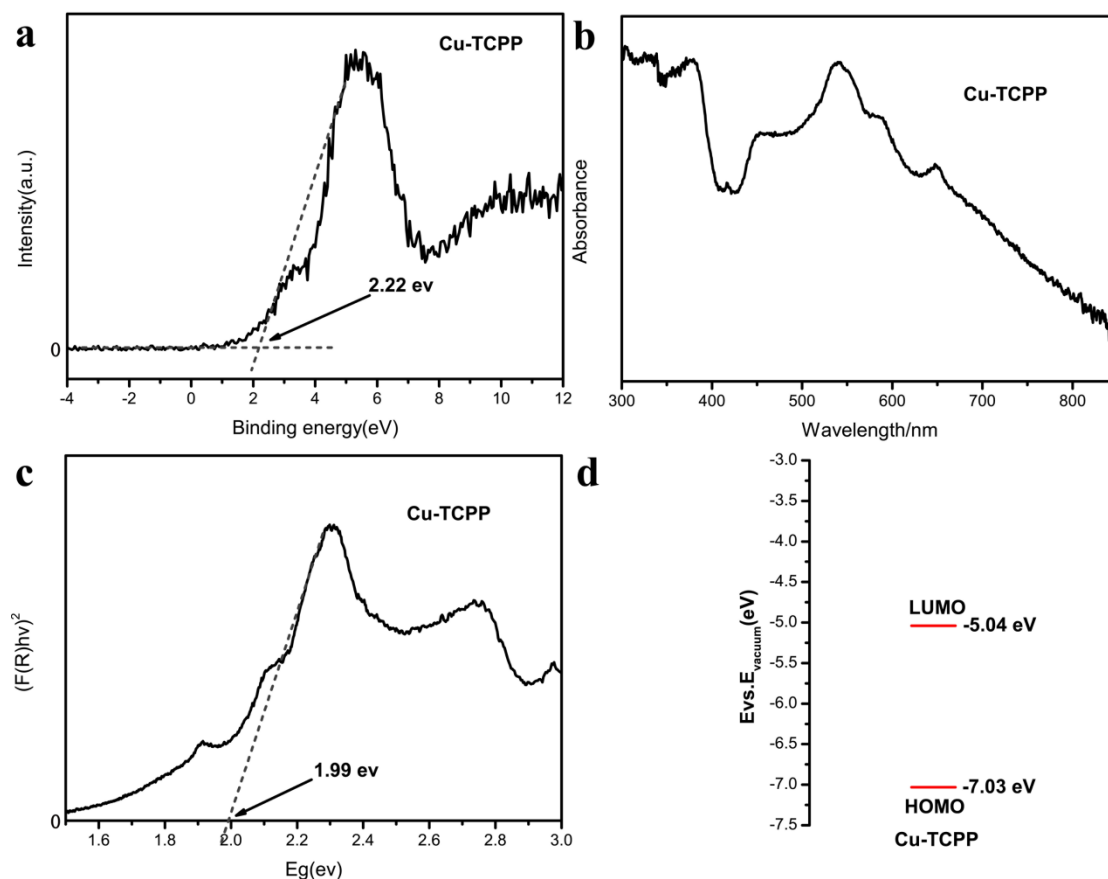


**Figure. S23** (a) Valence-band XPS spectrum of Cu-TCPP MOFs. The HOMO position of Cu-TCPP MOFs is determined by linear extrapolation of the leading edges of the profile to the base line<sup>11-12</sup>. After calibration with the reference Fermi level, the HOMO value for Cu-TCPP MOFs is calculated to be 7.03 eV with respect to vacuum. (b) UV-Vis absorption spectrum and (c) a plot of the transformed Kubelka-Munk function versus the energy of the exciting light, giving a band-gap energy of 1.99 eV for Cu-TCPP MOFs. (d) Energy-level diagram of Cu-TCPP MOFs. Based on the energy values of the HOMO level and band-gap, the LUMO level of Cu-TCPP MOFs is determined to be about -5.04 eV with respect to vacuum.

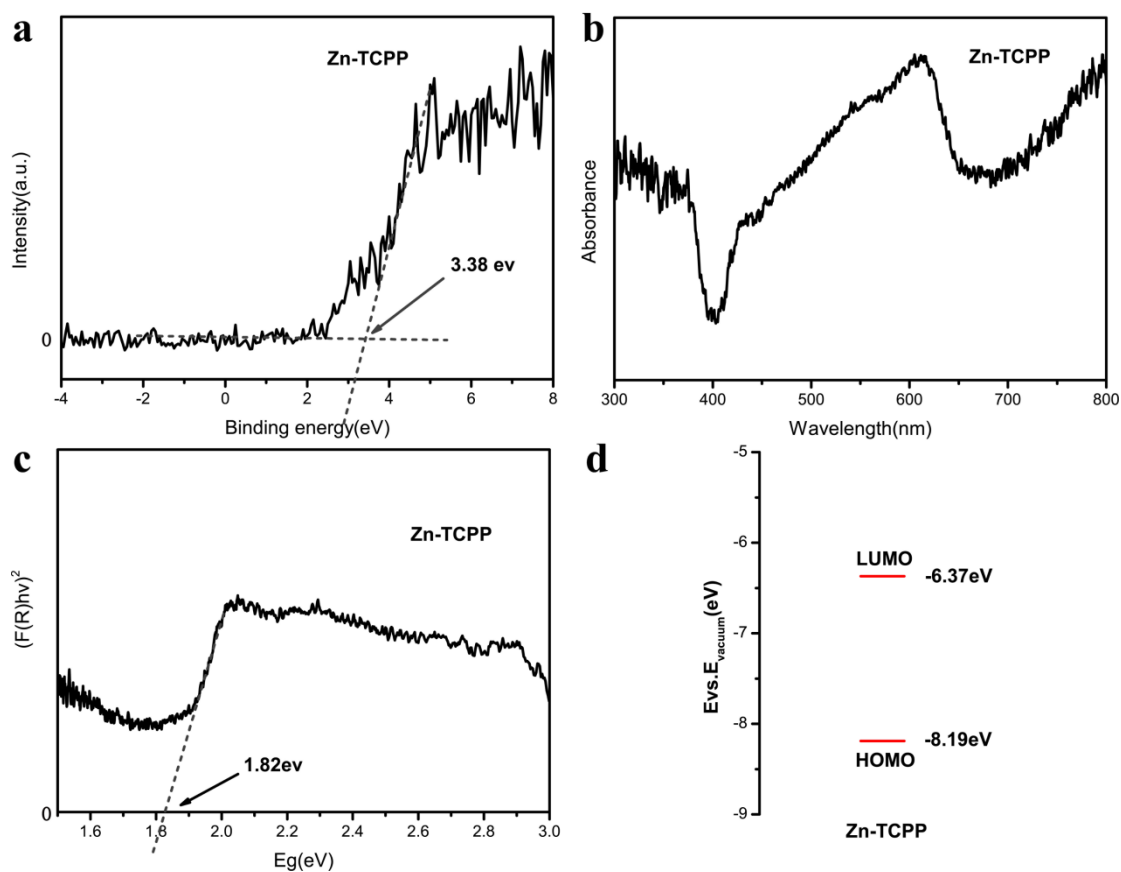


**Figure. S24** (a) Valence-band XPS spectrum of Zn-TCPP MOFs. The HOMO position of Zn-TCPP MOFs is determined by linear extrapolation of the leading edges of the profile to the base line<sup>11-12</sup>. After calibration with the reference Fermi level, the HOMO value for Zn-TCPP MOFs is calculated to be 8.19 eV with respect to vacuum. (b) UV-Vis absorption spectrum and (c) a plot of the transformed Kubelka-Munk function versus the energy of the exciting light, giving a band-gap energy of 1.82 eV for Zn-TCPP MOFs. (d) Energy-level diagram of Zn-TCPP MOFs. Based on the energy values of the HOMO level and band-gap, the LUMO level of Zn-TCPP MOFs is determined to be about -6.37 eV with respect to vacuum.

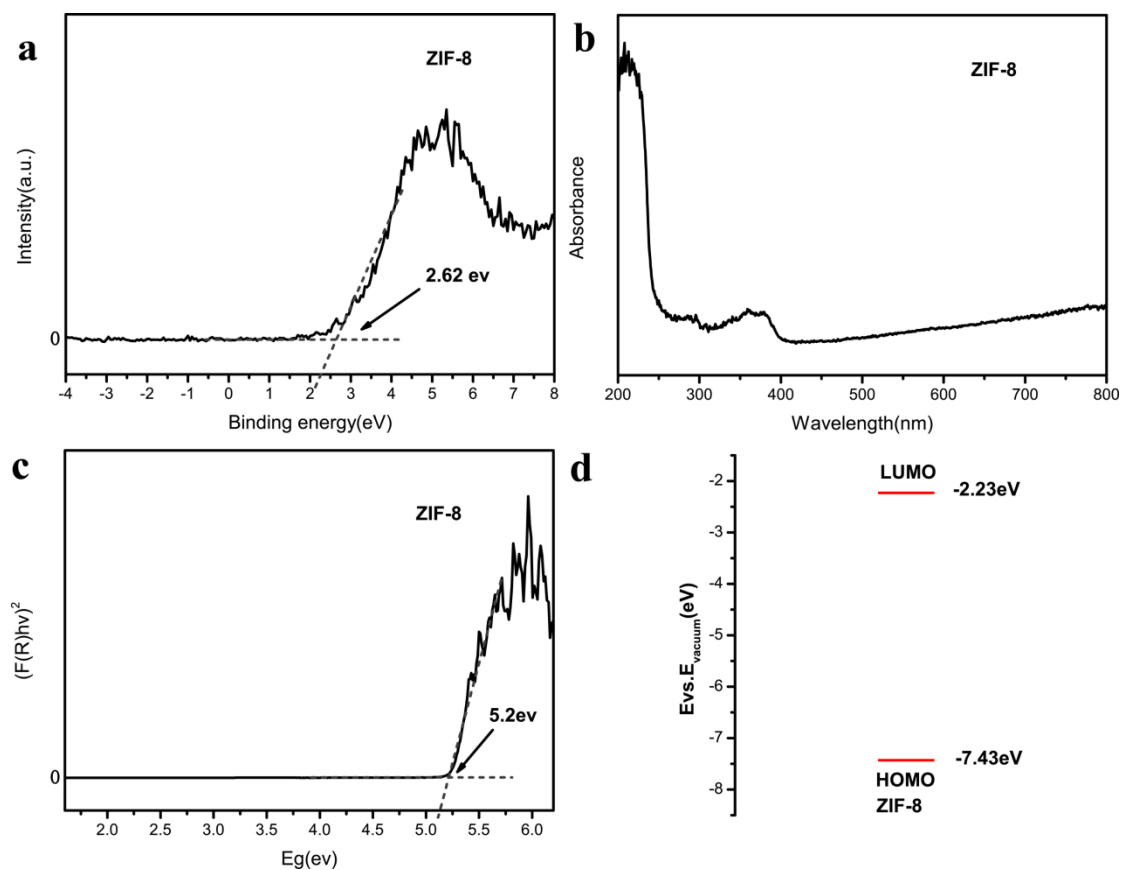


**Figure. S25** (a) Valence-band XPS spectrum of ZIF-8. The HOMO position of ZIF-8 is determined by linear extrapolation of the leading edges of the profile to the base line<sup>11-12</sup>. After calibration with the reference Fermi level, the HOMO value for ZIF-8 is calculated to be 7.43 eV with respect to vacuum. (b) UV-Vis absorption spectrum and (c) a plot of the transformed Kubelka-Munk function versus the energy of the exciting light, giving a band-gap energy of 5.2 eV for ZIF-8. (d) Energy-level diagram of ZIF-8. Based on the energy values of the HOMO level and band-gap, the LUMO level of ZIF-8 is determined to be about -2.23 eV with respect to vacuum.

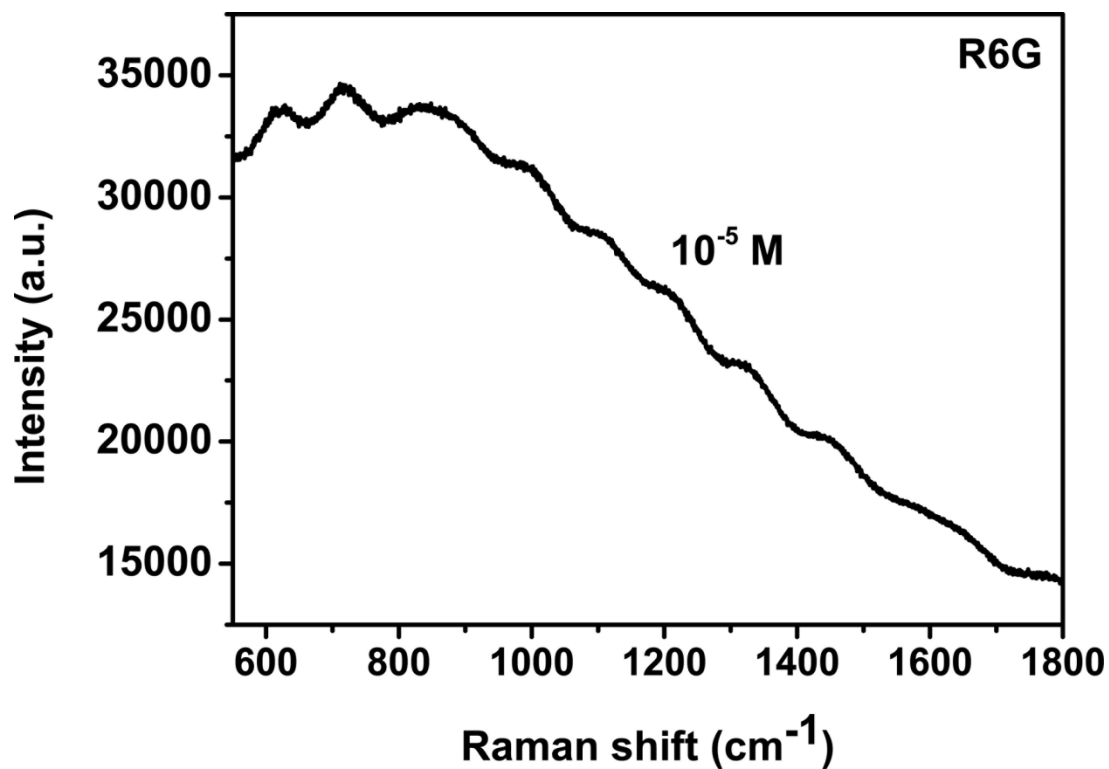


**Figure S26.** SERS spectrum of R6G at the concentration of  $10^{-5}$  M on the ZIF-67 substrate (tested in solution)

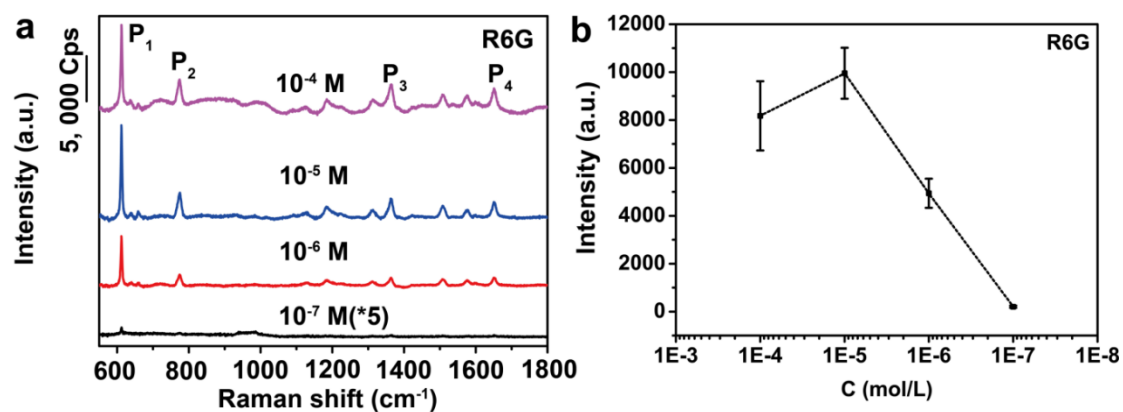


**Figure. S27 (a)** SERS spectra collected for the ZIF-67 substrate at four different concentrations,  $10^{-4}$ ,  $10^{-5}$ ,  $10^{-6}$ , and  $10^{-7}$  M, respectively. **(b)** A plot of SERS signal intensity versus R6G concentration ( $10^{-4}$ ~ $10^{-7}$  M) for the band at  $612\text{ cm}^{-1}$  on the ZIF-67 substrate.

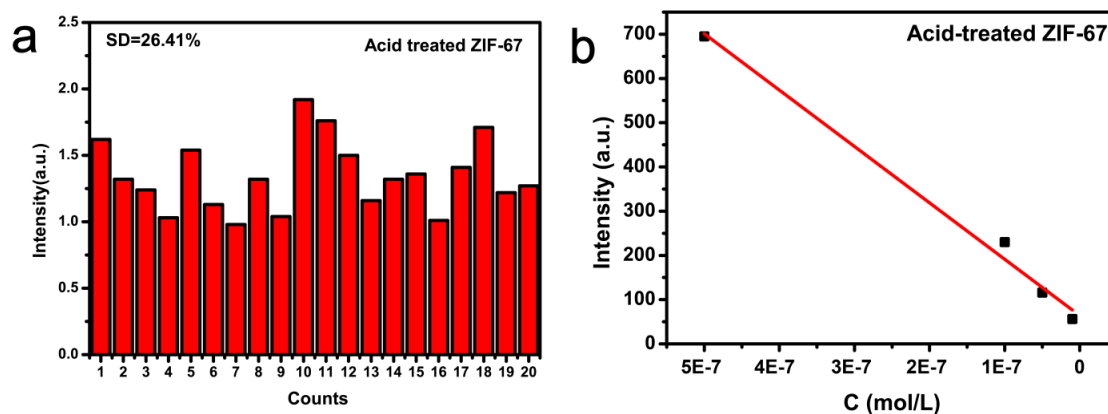


**Figure. S28** (a) The Raman signal intensities at  $612\text{ cm}^{-1}$  recorded for blank substrates of acid-treated ZIF-67 (without the loading of any analyte molecules). For each blank sample, data are acquired by recording 20 spectra from different substrates. The SD of the signal on the blank acid-treated ZIF-67 is calculated to be 26.4%. (b) A plot of SERS signal intensity versus R6G concentration ( $5 \times 10^{-7} \sim 10^{-8}\text{ M}$ ) for the band at  $612\text{ cm}^{-1}$  on the acid-treated ZIF-67 substrate.

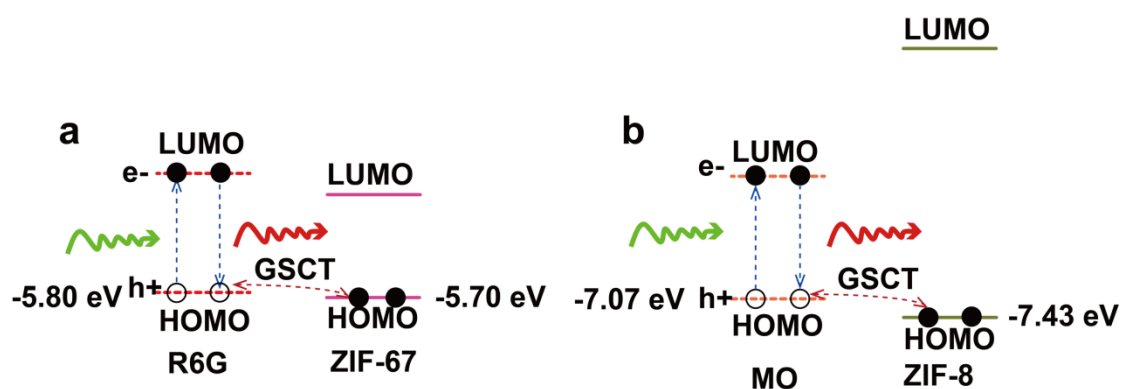


**Figure. S29** Schematic illustrating the GSCT process between analyte molecules and MOFs for (a) ZIF-67/R6G and (b) ZIF-8/MO system.

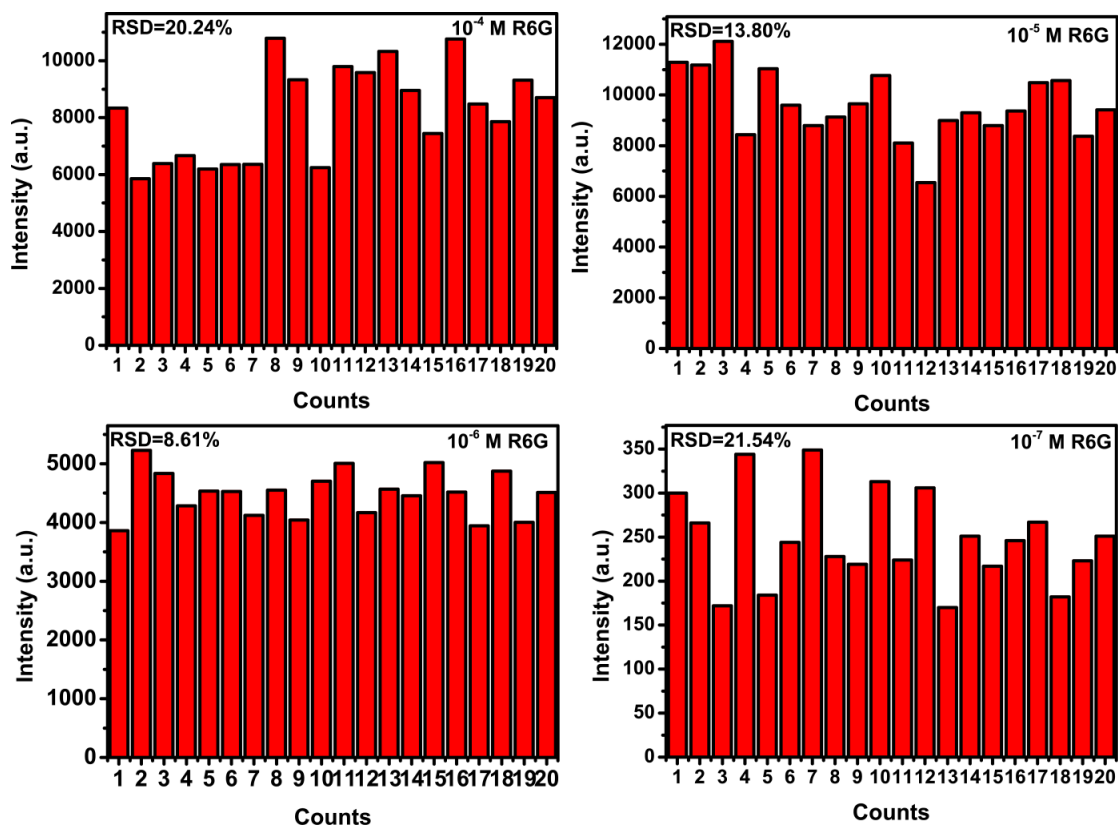


**Figure. S30** The intensities of the P<sub>1</sub> (612 cm<sup>-1</sup>) Raman vibration mode of R6G acquired from parallelly prepared ZIF-67 substrates at four different concentrations of R6G, namely 10<sup>-4</sup>, 10<sup>-5</sup>, 10<sup>-6</sup>, and 10<sup>-7</sup> M, respectively. 20 spectra from four different substrates (five stochastic spots per substrate) are acquired to estimate the reproducibility of the different substrates. The relative standard deviation (RSD) of the characteristic peak of R6G at 612 cm<sup>-1</sup> is used to estimate the reproducibility of the SERS signal. The RSDs of the P<sub>1</sub> mode of R6G at the four different concentrations, (10<sup>-4</sup>, 10<sup>-5</sup>, 10<sup>-6</sup>, and 10<sup>-7</sup> M) are calculated to be 20.2%, 13.8%, 8.6%, and 21.5%, respectively, indicating good reproducibility.

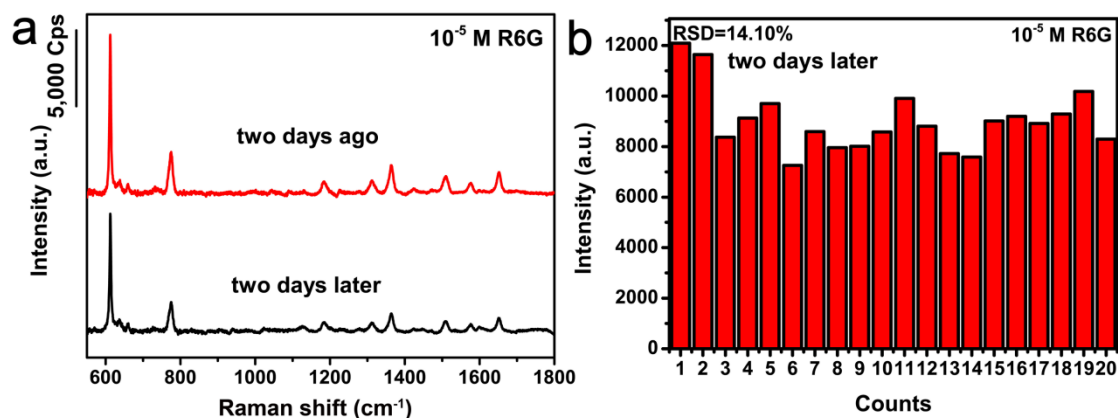


**Figure. S31** (a) SERS performances of the ZIF-67 samples obtained before/after two days of storage in the open air, for the detection of  $10^{-5}$  M R6G. It is noted that neither a shift in the major Raman peaks nor a significant change in the Raman intensity occurs for two days of storage, and (b) the RSD value remains as low as 14.1%.

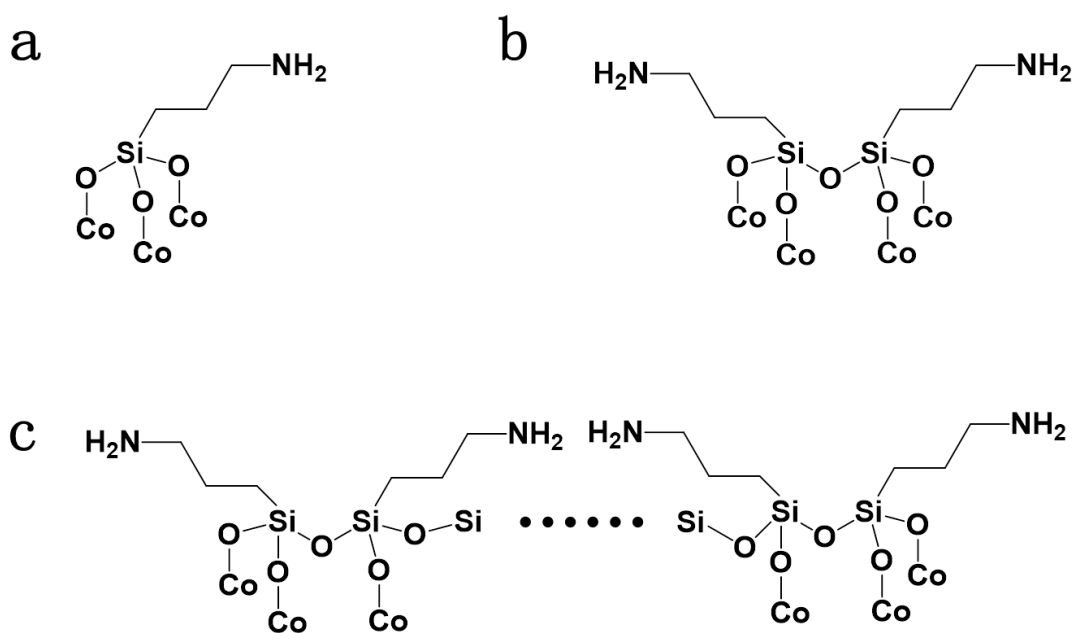


**Figure S32.** Schematic of the chemical bonding between silyloxy group and Co sites for the modification of ZIF-67 with APTES monomers.

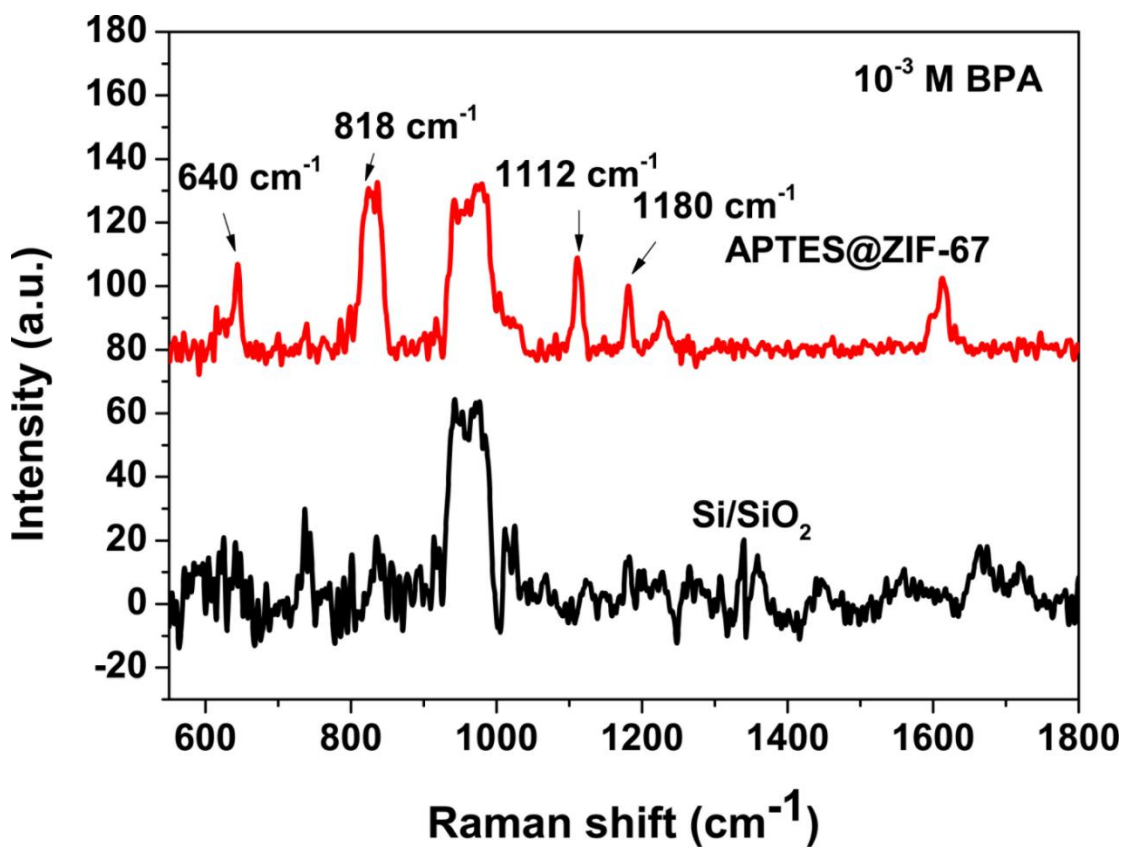


**Figure S33.** SERS spectra for BPA ( $10^{-3}$  M) on the APTES@ZIF-67 and bare Si/SiO<sub>2</sub> substrates.

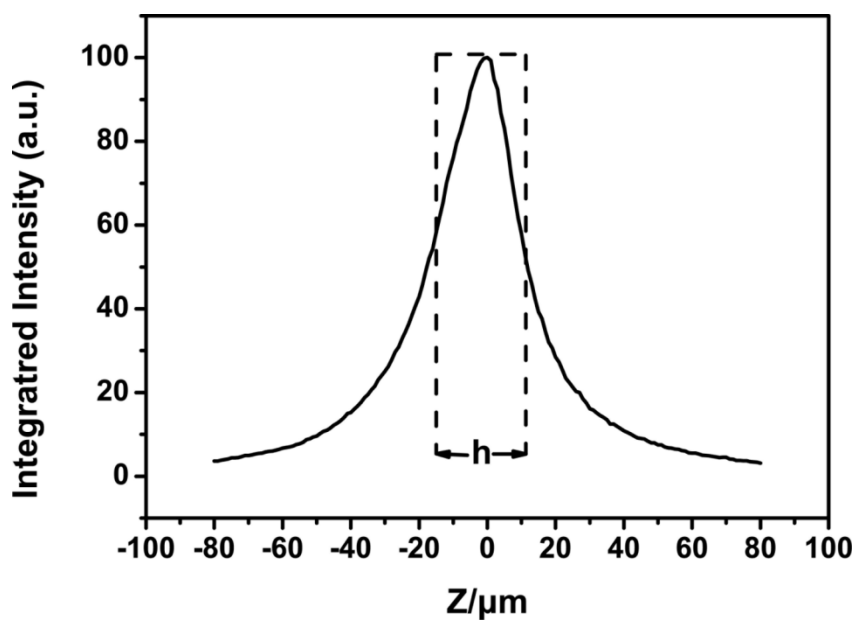


**Figure S34.** Raman intensity-depth profile determined by plotting the integrated

intensity of  $520.6\text{ cm}^{-1}$  band for a silicon wafer against the distance of the silicon wafer deviating from the ideally focused plane. The pinhole size of  $200\text{ }\mu\text{m}$  and a  $50\times$  long working-length objective are used.

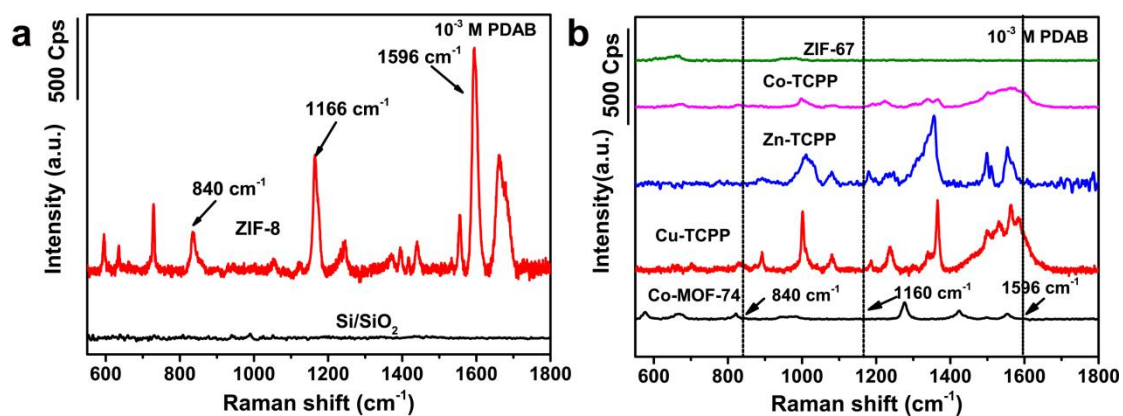


**Figure S35** SERS spectra for PDAB ( $10^{-3}\text{ M}$ ) on the (a) ZIF-8 substrate, (b) ZIF-67, Co-TCPP, Zn-TCPP, Cu-TCPP, and Co-MOF-74 substrates.

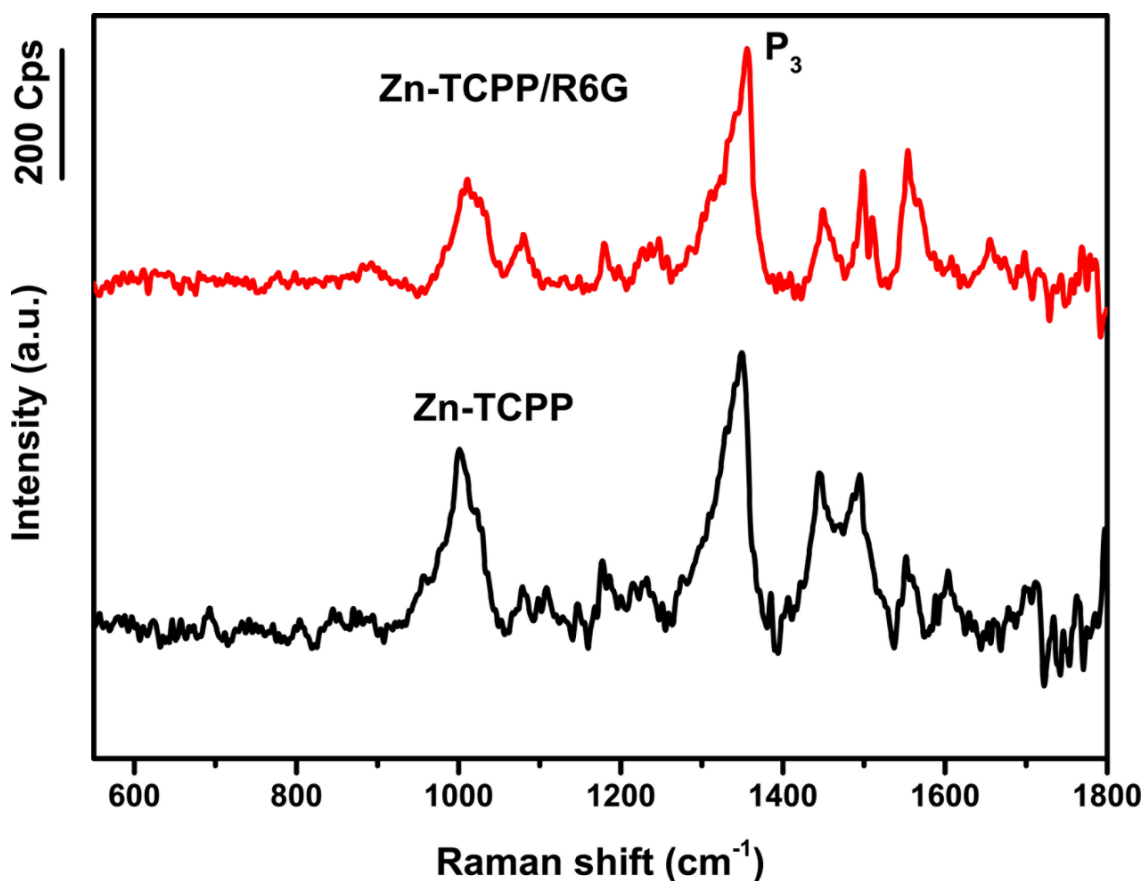


**Figure. S36** Raman spectra of the Zn-TCPP substrate with and without the loading of R6G analyte.

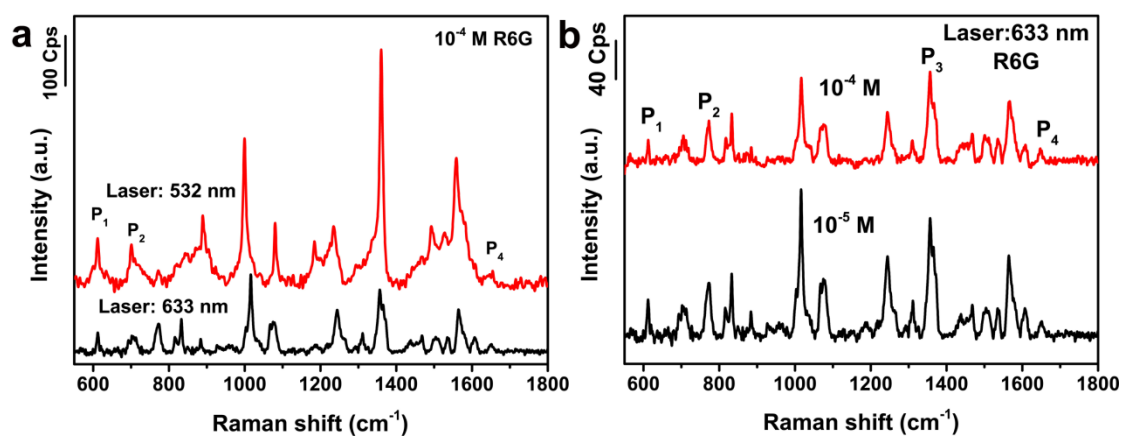


**Figure. S37** (a) SERS spectra of R6G on the Cu-TCPP substrate at the concentration of 10<sup>-4</sup> M, when excited by 532 and 633 nm lasers. (b) SERS spectra of R6G on the Cu-TCPP substrate at two different concentrations, 10<sup>-4</sup> and 10<sup>-5</sup> M, when excited by

633 nm laser.

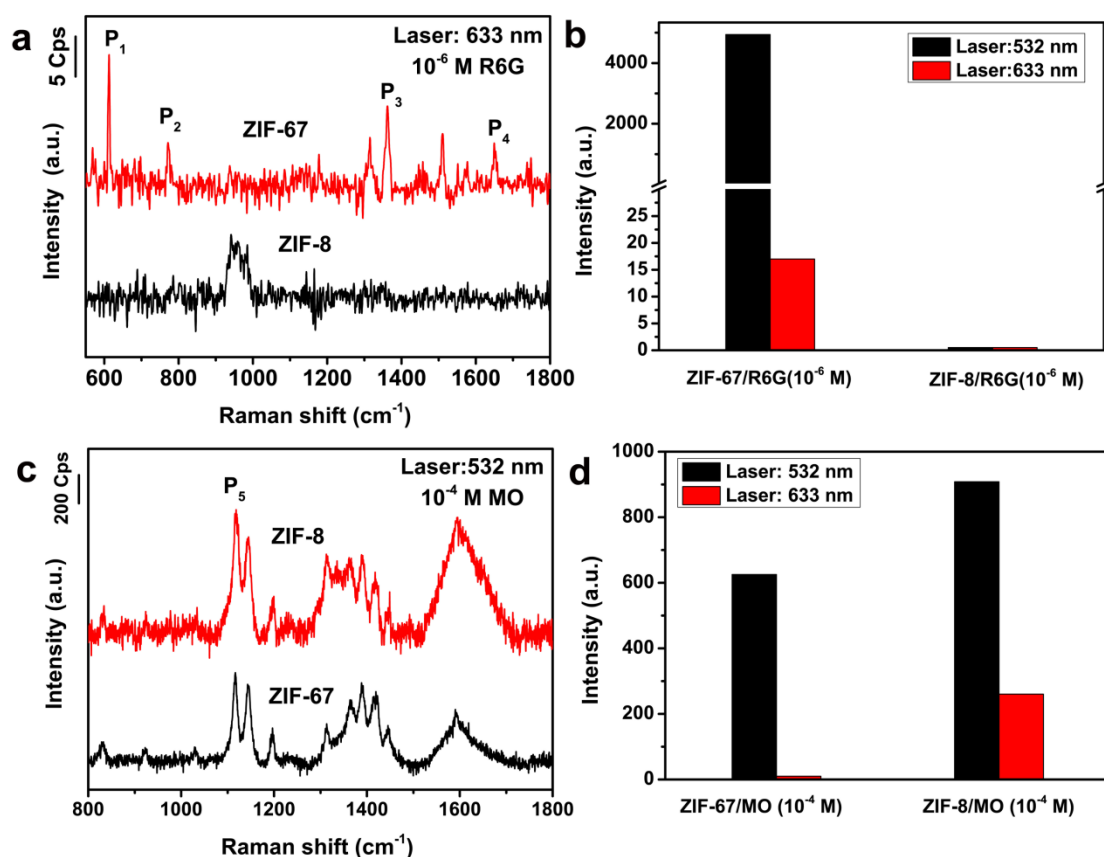


**Figure. S38** (a) SERS spectra of R6G ( $10^{-6}$  M) on the ZIF-67 and ZIF-8 substrates when excited by 633 nm laser. (b) A comparison of SERS activity between ZIF-67 and ZIF-8 under 532 and 633 nm laser excitations, based on the intensity of vibrational band at  $612\text{ cm}^{-1}$  of R6G. (c) SERS spectra of MO ( $10^{-4}$  M) on the ZIF-67 and ZIF-8 substrates when excited by 532 nm laser. (d) A comparison of SERS activity between ZIF-67 and ZIF-8 under 532 and 633 nm laser excitations, based on the intensity of vibrational band at  $1115\text{ cm}^{-1}$  of MO.

**Table S1.** Elemental composition of APTES@ZIF-67 obtained by ICP-OES analysis.

APTES@ZIF-67	Co	Si	ZIF-67	APTES
wt%	15.96	2.22	89.38	10.62

### Supplementary Note S1. Sampling approaches

In general, three typical sampling approaches have been used to obtain SERS spectra of analytes adsorbed on SERS substrates in powder form in many of the references. One approach is to soak the SERS substrates in a solution of analytes (soaking method)<sup>14</sup>. The SERS substrates are then centrifuged and rinsed with water to remove excess analytes. In the second approach, analytes and SERS substrates are mixed together and the mixture solution is then dropped and dried onto a cleaned silicon wafer (mixing method)<sup>15-16</sup>. For the third approach, the analytes are spread on the pretreated SERS substrates (drop-casting method)<sup>17-18</sup>. In contrast, obtaining SERS spectra by directly measuring the analyte-SERS substrate suspension solution is not usually used, to the best of our knowledge, probably due to the large dissipation of laser during its penetrating through the suspension solution that results in low detection limits and large fluorescence backgrounds (Figure S26).

Comparing with soaking method and mixing method, more reproducible data acquisition could be obtained using drop-casting method in our present system, so we finally resort to the drop-casting method, a widely reported method especially suitable for powder materials as SERS substrates<sup>15-16</sup>, in our SERS detection based on MOF materials. To further minimize the influences of coffee-ring effect, two specific

strategies are introduced: (1) SERS spectra are acquired from the inner area of the casting film with a relatively uniform distribution, but not from the droplet edge caused by the coffee-ring effect, similar to the case reported by Xu et al<sup>19</sup>. (2) Although the situation in a real micro-Raman experiment may be complicated, EF calculation is still necessary for the selection of substrate, since it may be the only reference we can appeal for the performance evaluation between different substrates. Also, we have improved the EF calculation by averaging the SERS mapping signals to minimize the random cause, as described in Figure S4-S7 and S10.

### Supplementary Note S2. The confocal depth (h) of the laser beam

The calculation of the enhancement factor (*EF*) in our work is detailed as follows:

$$EF=(I_{\text{SERS}}/N_{\text{SERS}})/(I_{\text{bulk}}/N_{\text{bulk}}) \quad (1)$$

$$N_{\text{SERS}}=CVN_{\text{A}}A_{\text{Raman}}/A_{\text{Sub}} \quad (2)$$

$$N_{\text{bulk}}=\rho hA_{\text{Raman}}N_{\text{A}}/M \quad (3)$$

where  $I_{\text{SERS}}$  and  $I_{\text{bulk}}$  are the intensities of the selected Raman peak in the SERS and normal Raman spectra, and  $N_{\text{SERS}}$  and  $N_{\text{bulk}}$  are the average number of molecules in the scattering area of the SERS and non-SERS substrates, respectively. Here the data for R6G (0.05 M) on bare Si/SO<sub>2</sub> substrate were used as non-SERS-active reference. Specifically, the intensity was obtained by taking average from measurements of 20 spots, and the number of analyte molecules ( $N_{\text{SERS}}$ ) was estimated by Supplementary equation 2 on the assumption that the analyte molecules were distributed uniformly on the substrates.  $C$  is the molar concentration of the analyte solution,  $V$  is the volume of the droplet, and  $N_{\text{A}}$  is the Avogadro constant.  $A_{\text{Raman}}$  is the laser spot area (1  $\mu\text{m}$  in

diameter) of the Raman scanning. 20  $\mu\text{L}$  of the analyte solution was spontaneously spread into a circle of about 3 mm in diameter on the substrate after solvent evaporation, from which the effective area of the substrate,  $A_{\text{Sub}}$ , can be obtained. On the other side,  $N_{\text{bulk}}$  can be calculated by Supplementary equation 3 on the basis of molecular weight ( $M$ ) and density ( $\rho$ ) of bulk R6G ( $1.15 \text{ g cm}^{-3}$ ) and the confocal depth ( $h$ ) of the laser beam.

For the confocal depth ( $h$ ) of the laser beam, recent references give different values for solid bulk crystalline R6G from 10, 13, 21 to 26  $\mu\text{m}$ <sup>20-23</sup>, which might be related to different pinhole sizes and objective lens of their used Raman instruments. To provide a more accurate estimate of the confocal depth in our system, a Raman intensity-depth profile of the  $520.6 \text{ cm}^{-1}$  band for a silicon wafer has been made in the light of the model assumed by Cai et al.<sup>22</sup> (Figure S34). Judging from the profile, the confocal depth ( $h$ ) is determined to be 23.64  $\mu\text{m}$  in our system, in contrast to the one previously used (21  $\mu\text{m}$ ).

### **Supplementary Note S3. Relationship between SERS signal intensity and R6G concentration**

We have added a new plot of SERS signal intensity versus R6G concentration ( $10^{-4} \sim 10^{-7} \text{ M}$ ) for the band at  $612 \text{ cm}^{-1}$  on the ZIF-67 substrate (Figure S27b). From the plot, it is clear that there is a positive correlation between the Raman intensity and the R6G concentration in the concentration range from  $10^{-7}$  to  $10^{-5} \text{ M}$ , and a negative one at a concentration larger than  $10^{-5} \text{ M}$  (Figure S27b). Such a negative correlation

can be explained by the shading effect of the analytes at high analyte concentrations. In fact, since the chemical mechanism determined by the charge transfers between analyte molecules and MOF materials is believed to mainly contribute to the SERS effect on MOF materials, the direct contacts between analyte molecules and MOF materials are needed to achieve SERS enhancement. Accordingly, it can be inferred that the largest enhancement may be observed when maximum monolayer adsorption of analyte molecules on the surface of SERS substrates is achieved, while further loading of analyte would cause a detrimental effect on SERS enhancement due to the shading effect of the analytes. To avoid such suppressing effect on the Raman intensity at high analyte concentrations, the adsorption isotherm for R6G onto MOF substrate are plotted (as shown in Figure S3), from which it can be roughly estimated that a sub-monolayer adsorption of R6G molecule onto the MOF substrate can be reached at an initial R6G concentration lower than  $3.4 \times 10^{-4}$  M. Therefore, to ensure a monolayer coverage of analyte on the substrate surface, a R6G concentration of  $10^{-6}$  M is chosen for the EF calculation in the present work, except for Co-MOF-74 using a concentration of  $10^{-5}$  M, since no conspicuous signals can be obtained with Co-MOF-74 substrate at R6G concentration of  $10^{-6}$  M.

#### **Supplementary Note S4. Discussion about the SERS enhancement mechanism between Co-MOF-74 and Cu-TCPP MOFs**

In the case of Co-MOF-74, there are two kinds of photo-induced charge-transfer transitions (PICT) at energies of 1.43 and 2.68 eV between analyte molecules and

SERS substrate, neither of which is close to the excitation laser energy for resonance, explaining the observed weak SERS activity of Co-MOF-74 under 532 nm laser excitation. As for Cu-TCPP MOFs, its poor SERS enhancement can also be explained in terms of the two types of charge-transfer transitions at the energies of 0.66 and 3.63 eV, both of which are far from the excitation laser energy ( $\lambda_L=2.33$  eV). However, the photo-induced charge-transfer transition is not the only reason for the different SERS enhancement among MOFs, especially when it is out of effective resonance with the incident laser. Other thermodynamically feasible resonances, such as the interband transition involving the creation of an electron–hole pair within MOFs (1.81 eV for Co-MOF-74 and 1.99 eV for Cu-TCPP MOFs), may be other factors responsible for the slight difference in SERS performances between Co-MOF-74 and Cu-TCPP MOFs, which may contribute to the overall Raman enhancement through intensity borrowing based on the Herzberg-Teller vibronic coupling.

### Supplementary Note S5. Herzberg–Teller coupling term<sup>24</sup>

A-Terms. Molecule to Substrate Charge Transfer

$$R_{ICK}(\omega) = \frac{\mu_{KI}\mu_{IC}h_{CK}\langle i|Q_K|f\rangle}{((\epsilon_1(\omega) + 2\epsilon_0)^2 + \epsilon_2^2(\omega))((\omega_{IC}^2 - \omega^2) + \gamma_{IC}^2)((\omega_{KI}^2 - \omega^2) + \gamma_{KI}^2)}$$

1

$$R_{ICV}(\omega) = \frac{\mu_{VC}\mu_{IC}h_{IV}\langle i|Q_K|f\rangle}{((\epsilon_1(\omega) + 2\epsilon_0)^2 + \epsilon_2^2(\omega))((\omega_{IC}^2 - \omega^2) + \gamma_{IC}^2)((\omega_{VC}^2 - \omega^2) + \gamma_{VC}^2)}$$

2

B-Terms. Substrate to Molecule Charge Transfer

$$R_{IVK}(\omega) = \frac{\mu_{VK}\mu_{KI}h_{IV}\langle ilQ_K|f\rangle}{((\varepsilon_1(\omega) + 2\varepsilon_0)^2 + \varepsilon_2^2(\omega))((\omega_{VK}^2 - \omega^2) + \gamma_{VK}^2)((\omega_{KI}^2 - \omega^2) + \gamma_{KI}^2)}$$

3

$$R_{KVC}(\omega) = \frac{\mu_{CV}\mu_{VK}h_{KC}\langle ilQ_K|f\rangle}{((\varepsilon_1(\omega) + 2\varepsilon_0)^2 + \varepsilon_2^2(\omega))((\omega_{VK}^2 - \omega^2) + \gamma_{VK}^2)((\omega_{CV}^2 - \omega^2) + \gamma_{CV}^2)}$$

4

### Supplementary Note S6. Discussion about the SERS enhancement mechanism between Co-MOF-74 and ZIF-8

In the case of Co-MOF-74, there are two kinds of photo-induced charge-transfer transitions (PICT) at energies of 1.43 and 2.68 eV between analyte molecules and SERS substrate, neither of which is close to the excitation laser energy for resonance, explaining the observed weak SERS activity of Co-MOF-74 under 532 nm laser excitation. As for the ZIF-8/MO system, the ground-state charge-transfer (GSCT) transition plays a more decisive role in the SERS detection of MO with ZIF-8. The GSCT, referring to the fact that even in the ground state there exists a charge transfer between the aligned energy levels of SERS substrate and analyte, can also contribute to an increased polarizability of the analyte molecules and thus improving SERS signals<sup>25</sup> (Figure S29). In the ZIF-8/MO system, the HOMO level of ZIF-8 is located at -7.43 eV, close to that of MO (-7.07 eV), so GSCT may be expected to occur (Figure S29).

### Supplementary Note S7. The role of charge-transfer transition in the selectivity and tailorability of MOF based SERS substrate

The charge-transfer resonance, which is in close relationship with the photo-induced charge transfer between the band edges of the SERS substrate and the affinity levels of the adsorbed analyte, typically comprises the core of MOFs-mediated SERS enhancement. Strong SERS enhancements for specific analytes can only occur when ensuring high-efficiency charge-transfer process. Otherwise, there will be no SERS signal observable for the analytes. Thus, charge-transfer transition plays a crucial role in the selectivity and tailorability of MOF-based SERS substrates.

Tailoring the band structures of MOFs by modifying the metal centers, ligands and surface groups of MOFs is indispensable to adjusting the overall charge-transfer efficiency and then the selective SERS effect. As a demonstration of the concept, MOFs (ZIF-67 and ZIF-8) with distinct band levels are designed, which has been proved to be suitable for the selective SERS detection of different analytes (R6G and MO), with their SERS performances successfully illustrated by the role of band structure matching. The tailorability of the band structure of MOFs and their selectivity in SERS detection have initiated our work on MOFs-based SERS, which will be further enriched with more detailed studies, such as the MOFs with different crystalline structure and surface groups, the interaction between the metal center, ligand and the analyte.

## **Supplementary Note S8. The advantage of MOFs-based substrates for surface modification**

Compared with classical noble metal-based SERS substrates, the key advantage of MOFs-based substrates for surface modification is that MOFs have strong bonding capability and versatile coordination modes, featured by strongly designable surface groups that can be combined with different modifiers, which allows the easy grafting of the modifiers to the MOF surfaces. In contrast, noble metals are not versatile materials for surface modification, which can only be effectively modified with a very limited number of compounds with specific functional groups such as mercapto groups.

#### **Supplementary Note S9. The estimation of the detection limit for R6G**

In a recent review article<sup>26</sup> reported by A. Shrivastava and V. B. Gupta, three strategies have been introduced as the method of obtaining the Limit of detection (LOD), including (1) visual evaluation, (2) the calculation from the signal-to-noise ratio (S/N), and (3) the calculation from the calibration line at low concentrations.

In our present work, the first method of visual evaluation is adopted for the estimation of detection limit for R6G on MOFs, that is, a rough detection limit for R6G is determined from the lowest concentration at which the signals of analytes can still be clearly noticed, which has been commonly used in the recent SERS literatures<sup>15, 17-18</sup>.

To assure correct understanding of the reviewer's comment, the value of limit of detection (LOD) is also estimated using other two methods. (1) The value of detection limit is estimated from the calibration line at low concentrations, based on the

relationship between the standard deviation of blank (sbl) and the slope of a calibrated curve (Figure S28 in Supporting Information). According to the method, the detection limit for acid-treated ZIF-67 is estimated to be  $6.24 \times 10^{-10}$  M, obviously lower than that measured by the lowest concentration of analyte with detectable signals. (2) The detection limit for R6G is also calculated based on the signal-to-noise ratio (S/N=3). The noise (N), is estimated from the Raman signal intensity at  $612 \text{ cm}^{-1}$  of blank acid-treated ZIF-67 substrates (without the loading of any analyte molecules) by the average of 20 spectra acquired from different spots, with the value calculated to be 1.34. Then, since the signal intensity for the band at  $612 \text{ cm}^{-1}$  on the acid-treated ZIF-67 substrate at R6G concentration of  $5 \times 10^{-9}$  M is just larger than 4.02 ( $3 \times N$ ), the detection limit for R6G can be determined to be  $5 \times 10^{-9}$  M.

### **Supplementary Note S10. The SERS effects of other toxic or important molecules.**

In addition to R6G, methyl orange and benzaldehyde, other types of molecules such as bisphenol A (BPA) and p-(dimethylamino)benzaldehyde have also been selected as analytes for SERS detection with MOF materials. Distinguishable SERS signals related to BPA ( $10^{-3}$  M) can be observed on APTES@ZIF-67 substrate, with four characteristic bands at 640, 818, 1112, and  $1180 \text{ cm}^{-1}$  for BPA (Figure S33). Noticeably, the selective SERS effect is also seen for PDAB adsorbed on different MOF substrates. Strong SERS signals for PDAB ( $10^{-3}$  M) can be detected from ZIF-8, but other MOFs show almost no detectable signals (Figure S35).

**Supplementary Note S11. The vibration band at about 1365 cm<sup>-1</sup> of TCPP-based MOFs.**

As is known, R6G can give a characteristic band at about 1360 cm<sup>-1</sup>, named as P<sub>3</sub>, which can be assigned to aromatic C–C stretching vibration modes<sup>27</sup>. However, Zn-TCPP MOFs also gives a main peak in a very similar position (about 1365 cm<sup>-1</sup>) (Figure S36), which is probably related to the aromatic C–C stretching vibration mode of Zn-TCPP MOFs<sup>28</sup>. In that case, P<sub>3</sub> must just overlap with the characteristic band of Zn-TCPP MOFs. It appears that the band overlapping also occurs for Co-TCPP MOFs and Cu-TCPP MOFs.

**Supplementary Note S12. The SERS performances of Cu-TCPP MOFs/R6G system at 633 nm laser excitation.**

The SERS signals from Cu-TCPP MOFs/R6G system are also obtained at an excitation wavelength of 633 nm, as shown in Figure S37. Clearly, the signals at 633 nm laser excitation are comparatively weaker than those at 532 nm laser excitation. A possible explanation for the observed signal difference is given as follows:

According to the chemical mechanism of SERS, The existence of photo-induced charge-transfer (PICT) transition with energy at or near that of incident laser for an effective resonance may be one of the premises for strong SERS enhancements based on MOFs. However, other thermodynamically feasible resonances such as interband transition within MOFs and molecular transition of analyte have also been found to

play crucial roles in the SERS enhancement of MOFs through vibronic coupling, according to the theory established by Lombardi et al<sup>29</sup>. On coupling, the relatively weak charge-transfer resonance borrows intensity from the stronger nearby resonances, which can be expressed by a Herzberg-Teller coupling term  $h_{CK}$  and  $h_{IV}$  for intensity borrowing from molecular and interband transitions, respectively (Supplementary Note S5). In the case of the Cu-TCPP MOFs/R6G system, there are two kinds of PICT transitions at energies of 3.63 and 0.66 eV, neither of which is close to the laser excitation energies of 532 nm (2.33 eV) or 633 nm (1.96 eV), indicating that Cu-TCPP MOFs cannot exhibit intense SERS signals from R6G under either 532 nm or 633 nm laser excitation. Therefore, the small difference in SERS enhancement between the two different laser excitations originates from other types of thermodynamically feasible resonances, such as interband transition within MOFs and molecular transition of analyte. In fact, although the excitation wavelength at 633 nm is energetically near the interband transition within Cu-TCPP MOFs (1.99 eV), it is off resonance with the molecular transition of R6G (2.30 eV) as perfectly fulfilled at 532 nm. Accordingly, when compared with that obtained at 532 nm laser excitation, the SERS enhancement of Cu-TCPP MOFs/R6G system is not further improved at 633 nm laser excitation, with a detection limit for R6G estimated to be  $10^{-5}$  M (Figure S37b).

**Supplementary Note S13. The SERS performances of MOFs at two different excitation wavelengths (532 nm and 633 nm).**

The SERS performances of MOFs have been carefully analyzed using 532 nm and 633 nm incident wavelengths. For example, The SERS signals from Cu-TCPP MOFs/R6G system have been obtained at two different excitation wavelengths (532 nm and 633 nm), as shown in Figure S37. Clearly, the signals at 633 nm laser excitation are comparatively weaker than those at 532 nm laser excitation, and a possible explanation for the observed signal difference has been given in Supplementary Note S12. Moreover, the SERS spectra of R6G and MO at different excitation wavelengths (532 nm and 633 nm) on ZIF-67 and ZIF-8 have also been measured (Figure S38). As shown in Figure S38a, the characteristic vibrational bands of R6G ( $10^{-6}$  M) can be well discerned on ZIF-67 but not observed on ZIF-8 at 633 nm laser excitation, showing similar trends at 532 nm laser excitation. However, the SERS signals of R6G are greatly weakened at 633 nm laser excitation when compared with those obtained at 532 nm laser excitation (Figure S38b), which is probably due to the energetic off-resonance for both PICT transition (2.40 eV) and molecule transition (2.30 eV) in such a system with a 633 nm excitation laser (1.96 eV). As for the MO system, the characteristic vibrational band of MO ( $P_5$ ) appears at  $1115\text{ cm}^{-1}$  on both ZIF-67 and ZIF-8 at an excitation wavelength of 532 nm and 633 nm (Figure S38c and Figure 3c). Clearly, ZIF-8 always shows much stronger SERS signals compared with ZIF-67 at both excitation wavelengths (532 nm or 633 nm), demonstrating its superior SERS activity toward the SERS detection of MO analyte

over ZIF-67.

#### **Supplementary Note S14. Different types of resonances contributing to the SERS enhancement of MOFs**

We consider three types of resonances including the charge-transfer, exciton (or interband transition), and molecule resonances, together with the ground-state charge-transfer (GSCT) interactions, can contribute to the SERS enhancement of MOF substrates. As a matter of fact, the existence of photo-induced charge-transfer (PICT) transition with energy at or near that of incident laser for an effective resonance may be one of the major premises for strong SERS enhancements based on MOFs. On the other side, other thermodynamically feasible resonances such as interband transition within MOFs and molecular transition of analyte have also been found to play crucial roles in the SERS enhancement of MOFs through vibronic coupling, according to the theory established by Lombardi et al<sup>29</sup>. On coupling, the relatively weak charge-transfer resonance borrows intensity from the stronger nearby resonances, which can be expressed by a Herzberg-Teller coupling term  $h_{CK}$  and  $h_{IV}$  for intensity borrowing from molecular and interband transitions, respectively (Supplementary Note S5). In addition, the GSCT effect could also act as a possible contributor to the prominent SERS enhancement, when there is effective charge transfer between the aligned ground states of analyte and substrate.

## Supplementary Reference

1. Chen, Y. Z.; Wang, C.; Wu, Z. Y.; Xiong, Y.; Xu, Q.; Yu, S. H.; Jiang, H. L., From Bimetallic Metal-Organic Framework to Porous Carbon: High Surface Area and Multicomponent Active Dopants for Excellent Electrocatalysis. *Adv. Mater.* **2015**, *27* (34), 5010-5016.
2. Zhao, M.; Wang, Y.; Ma, Q.; Huang, Y.; Zhang, X.; Ping, J.; Zhang, Z.; Lu, Q.; Yu, Y.; Xu, H.; Zhao, Y.; Zhang, H., Ultrathin 2D Metal-Organic Framework Nanosheets. *Adv. Mater.* **2015**, *27* (45), 7372-7378.
3. Cho, H.-Y.; Yang, D.-A.; Kim, J.; Jeong, S.-Y.; Ahn, W.-S., CO<sub>2</sub> adsorption and catalytic application of Co-MOF-74 synthesized by microwave heating. *Catal. Today* **2012**, *185* (1), 35-40.
4. Koo, J.; Hwang, I. C.; Yu, X.; Saha, S.; Kim, Y.; Kim, K., Hollowing out MOFs: hierarchical micro- and mesoporous MOFs with tailorable porosity via selective acid etching. *Chem. Sci.* **2017**, *8* (10), 6799-6803.
5. Kresse, G.; Furthmüller, J., Efficient iterative schemes for ab initio total-energy calculations using a plane-wave basis set. *Phys. Rev. B Condens Matter* **1996**, *54* (16), 11169-11186.
6. Cong, S.; Yuan, Y.; Chen, Z.; Hou, J.; Yang, M.; Su, Y.; Zhang, Y.; Li, L.; Li, Q.; Geng, F.; Zhao, Z., Noble metal-comparable SERS enhancement from semiconducting metal oxides by making oxygen vacancies. *Nat. Commun.* **2015**, *6*, 7800.
7. Liu, C.-S.; Li, B.-H.; Chen, C.-H.; Peng, J.-W.; Lee, S., Enhancement in SERS

- intensities of azo dyes adsorbed on ZnO by plasma treatment. *J. Raman Spectros.* **2014**, *45* (5), 332-337.
8. Xie, L.; Ling, X.; Fang, Y.; Zhang, J.; Liu, Z., Graphene as a substrate to suppress fluorescence in resonance Raman spectroscopy. *J. Am. Chem. Soc.* **2009**, *131* (29), 9890-9891.
9. Nijem, N.; Kong, L.; Zhao, Y.; Wu, H.; Li, J.; Langreth, D. C.; Chabal, Y. J., Spectroscopic evidence for the influence of the benzene sites on tightly bound H<sub>2</sub> in metal-organic frameworks with unsaturated metal centers: MOF-74-cobalt. *J. Am. Chem. Soc.* **2011**, *133* (13), 4782-4784.
10. Yang, H.; Hu, H.; Ni, Z.; Poh, C. K.; Cong, C.; Lin, J.; Yu, T., Comparison of surface-enhanced Raman scattering on graphene oxide, reduced graphene oxide and graphene surfaces. *Carbon* **2013**, *62*, 422-429.
11. Chen, X.; Liu, L.; Yu, P. Y.; Mao, S. S., Increasing solar absorption for photocatalysis with black hydrogenated titanium dioxide nanocrystals. *Science* **2011**, *331* (6018), 746-750.
12. Li, L.; Yan, J.; Wang, T.; Zhao, Z. J.; Zhang, J.; Gong, J.; Guan, N., Sub-10 nm rutile titanium dioxide nanoparticles for efficient visible-light-driven photocatalytic hydrogen production. *Nat. Commun.* **2015**, *6*, 5881.
13. Yang, H.; He, X.-W.; Wang, F.; Kang, Y.; Zhang, J., Doping copper into ZIF-67 for enhancing gas uptake capacity and visible-light-driven photocatalytic degradation of organic dye. *J. Mater. Chem.* **2012**, *22* (41), 21849.
14. Zheng, K. H.; Chou, Y. C.; Wu, Y. J.; Lee, Y. T., Raman spectra of benzoic acid

enhanced by the silver nanoparticles of various sizes. *J. Raman Spectros.* **2009**, *41* (6), 632-635.

15. Zhang, Q.; Li, X.; Ma, Q.; Zhang, Q.; Bai, H.; Yi, W.; Liu, J.; Han, J.; Xi, G., A metallic molybdenum dioxide with high stability for surface enhanced Raman spectroscopy. *Nat. Commun.* **2017**, *8*, 14903.

16. Lin, J.; Shang, Y.; Li, X.; Yu, J.; Wang, X.; Guo, L., Ultrasensitive SERS Detection by Defect Engineering on Single Cu<sub>2</sub>O Superstructure Particle. *Adv. Mater.* **2017**, *29* (5), 1604797.

17. Yilmaz, M.; Babur, E.; Ozdemir, M.; Giesecking, R. L.; Dede, Y.; Tamer, U.; Schatz, G. C.; Facchetti, A.; Usta, H.; Demirel, G., Nanostructured organic semiconductor films for molecular detection with surface-enhanced Raman spectroscopy. *Nat. Mater.* **2017**, *16* (9), 918-924.

18. Tao, L.; Chen, K.; Chen, Z.; Cong, C.; Qiu, C.; Chen, J.; Wang, X.; Chen, H.; Yu, T.; Xie, W.; Deng, S.; Xu, J. B., 1T' Transition Metal Telluride Atomic Layers for Plasmon-Free SERS at Femtomolar Levels. *J. Am. Chem. Soc.* **2018**, *140* (28), 8696-8704.

19. Zhou, J.; Xu, S.; Xu, W.; Zhao, B.; Ozaki, Y., In situ nucleation and growth of silver nanoparticles in membrane materials: a controllable roughened SERS substrate with high reproducibility. *J. Raman Spectros.* **2009**, *40* (1), 31-37.

20. Jiang, L.; You, T.; Yin, P.; Shang, Y.; Zhang, D.; Guo, L.; Yang, S., Surface-enhanced Raman scattering spectra of adsorbates on Cu<sub>2</sub>O nanospheres: charge-transfer and electromagnetic enhancement. *Nanoscale* **2013**, *5* (7), 2784-2789.

21. Chen, J.; Shen, B.; Qin, G.; Hu, X.; Qian, L.; Wang, Z.; Li, S.; Ren, Y.; Zuo, L., Fabrication of Large-Area, High-Enhancement SERS Substrates with Tunable Interparticle Spacing and Application in Identifying Microorganisms at the Single Cell Level. *J. Phys. Chem. C* **2012**, *116* (5), 3320-3328.
22. Cai, W. B.; Ren, B.; Li, X. Q.; She, C. X.; Liu, F. M.; Cai, X. W.; Tian, Z. Q., Investigation of surface-enhanced Raman scattering from platinum electrodes using a confocal Raman microscope: dependence of surface roughening pretreatment. *Surf. Sci.* **1998**, *406* (1), 9-22.
23. Zhang, Q.; Li, X.; Yi, W.; Li, W.; Bai, H.; Liu, J.; Xi, G., Plasmonic MoO<sub>2</sub> Nanospheres as a Highly Sensitive and Stable Non-Noble Metal Substrate for Multicomponent Surface-Enhanced Raman Analysis. *Anal. Chem.* **2017**, *89* (21), 11765-11771.
24. Lombardi, J. R.; Birke, R. L., Theory of Surface-Enhanced Raman Scattering in Semiconductors. *J. Phys. Chem. C* **2014**, *118* (20), 11120-11130.
25. Ling, X.; Moura, L. G.; Pimenta, M. A.; Zhang, J., Charge-Transfer Mechanism in Graphene-Enhanced Raman Scattering. *J. Phys. Chem. C* **2012**, *116* (47), 25112-25118.
26. Shrivastava, A.; Gupta, V., Methods for the determination of limit of detection and limit of quantitation of the analytical methods. *Chron. Young Scientists* **2011**, *2* (1), 21-25.
27. Hildebrandt, P.; Stockburger, M., Surface-enhanced resonance Raman spectroscopy of Rhodamine 6G adsorbed on colloidal silver. *J. Phys. Chem.* **1984**, *88*

(24), 5935-5944.

28. Cotton, T. M.; Schultz, S. G.; Van Duyne, R. P., Surface-enhanced resonance Raman scattering from water-soluble porphyrins adsorbed on a silver electrode. *J. Am. Chem. Soc.* **1982**, *104* (24), 6528-6532.

29. Alessandri, I.; Lombardi, J. R., Enhanced Raman Scattering with Dielectrics. *Chem. Rev.* **2016**, *116* (24), 14921-14981.